

for Modeling Quasi-Brittle Failure of Cohesive-Frictional Materials

M. Neuner^{a,*}, R. Regueiro^b, C. Linder^a

^a*Department of Civil and Environmental Engineering, Stanford University, Stanford, CA, USA*

^b*Department of Civil, Environmental, and Architectural Engineering, University of Colorado, Boulder, CO, USA*

Abstract

In this work, a novel framework for modeling quasi-brittle crack propagation and shear band dominated failure of cohesive-frictional materials like concrete, mortar, rock, tough ceramics, energetic materials, but also granular materials like sands or powders in terms of a unified continuum approach is proposed. It is based on a combination of the gradient-enhanced continuum with gradients of internal variables for representing quasi-brittle cracking, and the micropolar continuum, accounting for the deformation of the microstructure. For developing the gradient-enhanced micropolar framework, the set of balance equations and the kinematic relations are derived, and the constitutive relations are established in a general manner. The framework is formulated in a geometrically exact setting, based on the thermodynamically sound theory of hyperelasto-plasticity, and the numerical implementation by means of the finite element method is discussed. For assessing the approach, realizations of this new approach in terms of constitutive models for particular materials are developed. They are applied to numerical benchmark examples, investigating various loading conditions, and the obtained results are validated by means of a comparison with experiments from the literature.

Key words: Quasi-Brittle Fracture, Continuum Damage, Plasticity, Gradient-Enhanced Continuum, Micropolar Continuum

1. Introduction

Cohesive-frictional materials like concrete, mortar, rock, tough ceramics, energetic materials but also granular materials like sands or powders constitute an essential part of many engineering and scientific applications. The behavior of these materials, governed by *friction* and *cohesion* between particles or grains, is characterized by a highly nonlinear stress strain relationship. Common characteristics are (i) inelastic behavior that is observed even at low stress levels, (ii) low resistance in tension compared to a potentially high compressive strength, (iii) increasing material strength with increasing stress confinement, and (iv) complex failure mechanisms. In particular, in confined compression for many cohesive-frictional materials a rather ductile strain hardening behavior is followed by ductile strain softening, often accompanied by diffuse failure zones or highly localized zones of large inelastic deformations manifested by shear bands or fault zones, depending on the stress state. In contrast, certain frictional materials like sands do not sustain

*Corresponding author

Email addresses: neuner@stanford.edu (M. Neuner), richard.regueiro@colorado.edu (R. Regueiro), linder@stanford.edu (C. Linder)

Preprint submitted to International Journal of Solids and Structures

June 16, 2022

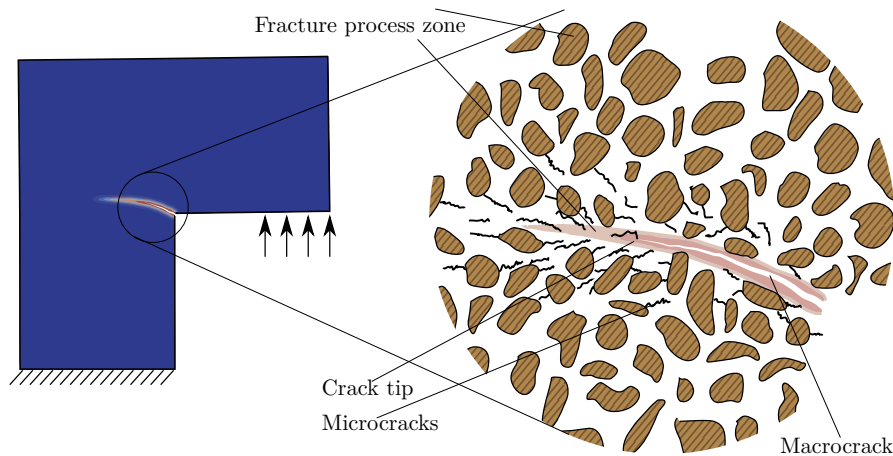


Figure 1: Failure in tension of cohesive-frictional materials is often observed in the form of quasi-brittle cracking, characterized by a failure process zone of finite size in which microcracks coalesce into a distinct macroscopic crack.

tensile stresses, whereas for other materials which exhibit cohesive bonds between particles, e.g., concrete or cemented granular materials, comparatively low tensile stresses lead to failure by cracking [53].

Accordingly, modeling the constitutive behavior of cohesive-frictional materials is a challenging task, and in this regard classical continuum models are often not sufficient. For classical continuum models, zones of localized large strains potentially arise due to softening material behavior, but also due to non-associated plastic flow. In models for cohesive-frictional materials based on the theory of plasticity, non-associated plastic flow rules are commonly required for representing the volumetric inelastic behavior in a realistic manner. From a numerical point of view, deficiencies related to material failure and localized inelastic deformations are encountered due to the loss of ellipticity of the underlying initial-boundary value problem for the static case, or the loss of hyperbolicity for dynamic problems, resulting in pathological mesh dependency in finite element simulations.

1.1. Quasi-brittle cracking of cohesive-frictional materials

For many cohesive-frictional materials with distinct cohesive particle bonds, softening material behavior in tension or unconfined compression results in discrete cracks. For such materials, the formation of cracks is characterized by a fracture process zone of finite size ahead of the crack tip, in which microcracks emerge and coalesce into a distinct stress free macroscopic crack (Figure 1) – a process which is commonly denoted as quasi-brittle cracking [10]. Due to the presence of a process zone with finite dimensions, quasi-brittle cracking is characterized by an inherent material length which is related to the microstructure of a material.

In classical continuum models, quasi-brittle failure is commonly represented by means of softening plasticity or continuum damage mechanics. However, such models exhibit several theoretical deficiencies [6]: (i) the fracture process zone is infinitesimally small, i.e., it has the size of a single material point, (ii) at the structural level, snapback behavior due to the infinitesimally small fracture process zone can be observed, and (iii) the amount of dissipated energy associated with fracture is zero due to the infinitesimal zone in which energy is dissipated. In finite element analyses, those deficiencies lead to a pathological mesh sensitivity: fracture tends to localize into the smallest possible domain, i.e., commonly a single layer of

finite elements, and upon mesh refinement, this localization zone decreases to an arbitrarily small domain. In other words, the obtained results are not objective with respect to the finite element mesh, i.e., they are sensitive to the numerical discretization scheme.

Objective, i.e., mesh insensitive, representation of softening material behavior is a vast subject of research, and in the past decades different approaches for regularizing softening material behavior in finite element simulations have been employed, e.g., the mesh-adjusted softening modulus [9, 84], the viscoplastic continuum [69], the integral nonlocal continuum [29, 85], as well as the implicit gradient-enhanced continuum [80] or the micromorphic continuum [28, 30]. In particular, so-called nonlocal continuum approaches, which are motivated by the micromechanical behavior of quasi-brittle materials [10], gained widespread acceptance. The term *nonlocal* is interpreted here in a broad sense [7], assuming that the response of a material point is not solely dependent on its own deformation history, but also on the state in a certain neighborhood. Among several different nonlocal approaches developed in the past decades, a well-established and in particular numerically attractive class of models for representing such nonlocal behavior is based on the theory of the implicitly gradient-enhanced continuum with gradients of internal variables. For such a model, the constitutive relations are enriched by spatial gradients of one or more thermodynamic damage-driving state variables, and additional balance relations in the form of higher order partial differential equations are incorporated into the continuum formulation [80]. This way, thermodynamically sound frameworks for describing quasi-brittle material failure can be formulated [32], which are also particularly amenable to efficient numerical implementations. Furthermore, it represents a proper remedy for the numerical issues related to softening material behavior in finite element simulations [54].

Many successful applications of the implicit gradient-enhanced continuum to cohesive-frictional materials are reported in the literature, for instance by Poh and Swaddiwudhipong [87] by means of an extended damage-plasticity model for concrete, which also served as the basis for a gradient-enhanced damage-plasticity model for rock mass [95]. A gradient-enhanced microplane model for concrete considering cyclic loading was presented by Zreid and Kaliske [115], and a model for concrete under high-temperature by Pearce et al. [79]. An application of the gradient-enhanced continuum to masonry was presented by Peerlings et al. [81]. Poh and Sun [86] proposed an model considering a decreasing interaction of microcracks with increasing damage, representing more realistically the transition to sharp macroscopic cracks. A general framework for dynamic quasi-brittle failure with microinertial effects was proposed recently by Wang et al. [111]. From a mathematical point of view, gradient-enhanced damage models formulations are closely related to phase field approaches for fracture [16], which have attracted considerable attention in the recent years.

In the context of finite strains and rotations, approaches for gradient-enhanced damage models were proposed by Liebe and Steinmann [62], Steinmann [99], for gradient-enhanced plasticity models by Liebe et al. [61], and for gradient-enhanced coupled damage-plasticity models by Areias et al. [4], Brepols et al. [11], Weisłó et al. [112]. Models for particular materials considering large strains were proposed for instance by Waffenschmidt et al. [110] for fiber-reinforced composites, by Hosseini et al. [46] for trabecular bone, and by Indriyantho et al. [48] for concrete. Finally, a comprehensive review on different gradient approaches for infinitesimal and finite strain plasticity was presented recently by Voyiadjis and Song [109].

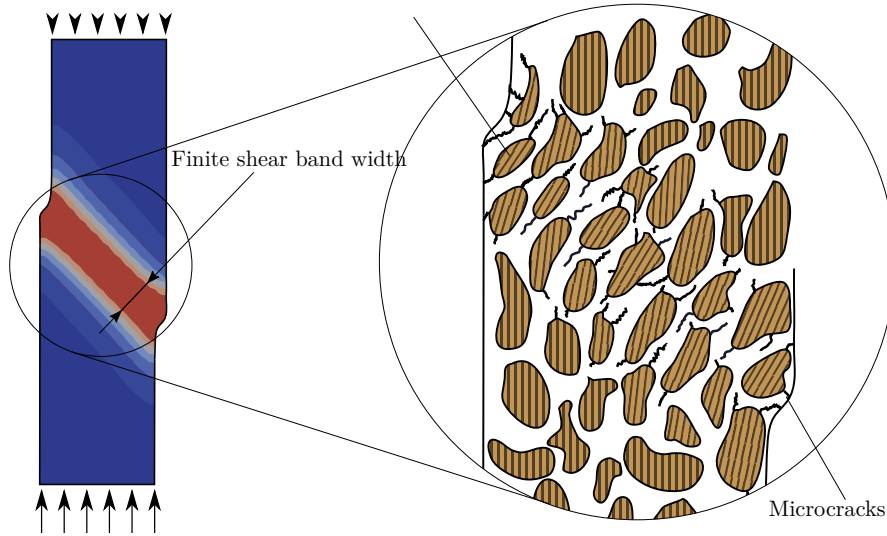


Figure 2: Shear bands in a cohesive-frictional material are characterized by a finite width, which is influenced by the deformation of microstructure of the material, e.g., the rotation of granular material particles. The rotation of these material particles is in general different from the macroscopically observed rotation of the structure.

1.2. Material Failure in Confined Compression and Shear

In contrast to the material behavior in tension, in confined compression and shear for many cohesive-frictional materials, highly localized zones of large inelastic deformations are observed, commonly in the form of shear bands or fault zones. Similar to quasi-brittle fracture zones, for such localized zones of inelastic deformations the size effect of cohesive-frictional materials becomes apparent, which is for instance manifested by the finite width of shear bands. Clearly, the characteristic dimensions of such localized zones are related to deformations of the microstructure of a material, for instance in the form of material particle rotations, depending on the scale of the microstructure or material heterogeneities (Figure 2).

Classical continuum models which lack any internal material length parameter cannot capture such localized zones of large strains properly. One possible alternative to the classical continuum is provided by the theory of the micromorphic continuum which emerged in the second half of the last century [28, 30]. It accounts for a deformable microstructure which contributes to the macroscopic behavior of a material. Considering a deforming microstructure leads to extended kinematic relations and higher order stress moments entering the balance relations. Such extended kinematic and balance relations, and additional constitutive relations for the microstructure result in characteristic material length scales inherent to the micromorphic continuum. Accordingly, a micromorphic continuum model accounts for material size effects in a natural way. One special case of the micromorphic continuum is the micropolar continuum [28]. For the micropolar continuum, the assumed deformation of the microstructure is restricted to a rotation, which can be envisioned as the average rotation of material particles.

The micropolar continuum emerged from the theoretical works by the Cosserat brothers [14] on a generalized continuum theory, which was later on investigated and extended by several authors [41, 67, 94, 106], and which is known today also as the so called Cosserat continuum. Kafadar and Eringen [57] extended the Cosserat continuum by including inertial effects, and formulated the Cosserat continuum as a special case of the general micromorphic continuum, which they denoted as the micropolar continuum. In contrast

to the classical Boltzmann continuum, which is characterized by a symmetric Cauchy stress tensor [108], the micropolar continuum is characterized by an, in general, nonsymmetric Cauchy stress tensor and an additional, in general, nonsymmetric couple stress tensor. By means of introduced characteristic material length scales, material size effects are captured in an implicit manner by the micropolar continuum [71]. Although the micropolar continuum received certain attention in particular in the geomechanics community [2, 22–24, 60, 63, 66, 68, 78, 101–105], only comparatively few applications are reported in other fields of engineering, e.g., [1, 42, 74, 75, 114]. This is due to several reasons, such as the complex nature of the micropolar formulation, the demanding computational effort in numerical simulations, and the limited experimental data on the material parameters, which still poses an issue [3, 44, 59]. Furthermore, already the determination of the basic elastic parameters is still focus of ongoing research endeavors [52, 71, 72].

For localized deformations involving particle rotations, for instance, the shear band width serves as the characteristic material length introduced by the micropolar continuum, which allows to overcome the mentioned issues inherent to the classical continuum. Furthermore, the micropolar continuum represents a proper countermeasure against pathological mesh dependency due to non-associated plastic flow in numerical simulations [15, 74].

In general, the highly ductile material behavior under confined compressive stress states resulting in large strains and rotations demands for a proper mathematical treatment within a geometrically exact setting. Approaches for the treatment of finite-strain hyperelastic-plastic models in the context of the classical continuum theory have been developed in the past decades, and are nowadays well-established in commercial and scientific numerical codes [17, 43, 97]. An extension of the hyperelastic-plastic approach to the micropolar continuum was proposed initially by Steinmann [98] based on a multiplicative decomposition of the microrotation tensor, with the implementation into a finite element framework discussed in [5]. Different approaches were proposed also by Forest et al. [34] for crystal plasticity, by Neff [70] considering a multiplicative decomposition of the macroscopic deformation gradient with microrotations restricted to elasticity, and by Grammenoudis and Tsakmakis [38, 39] using a similar approach as in [98] but considering additional kinematic hardening effects. A recent discussion on micropolar plasticity for large deformations can be found in [55].

While the micropolar continuum provides a physically sound framework for describing the observed size effect for localized deformations involving particle rotations, it fails to do so for cohesive failure in tension [19, 49, 100], which is not related to any rotation of the microstructure. In contrast, nonlocal approaches for quasi-brittle tensile failure, e.g., based on gradients of internal damage-driving state variables, which do not account for rotations of the microstructure, are potentially not sufficient for objectively describing the complex kinematics of shear band dominated softening behavior in numerical simulations, and moreover, they may not regularize structural softening behavior due to non-associated plastic flow [74].

For a general continuum model for cohesive-frictional materials, capable of representing material failure under a broad range of loading conditions, both the size effect related to microstructural deformations and the nonlocal character of quasi-brittle failure in terms of interacting microcracks must be taken into account.

This is the focus of the present work: We present a unified framework for modeling the mechanical behavior of cohesive-frictional materials, accounting for quasi-brittle failure and microstructural deformations, formulated in a geometrically exact, three-dimensional setting.

The proposed framework serves as basis for constitutive models for a broad range of engineering applications dealing with large, inelastic deformations and failure under various loading conditions, e.g., in geotechnics, tunnel construction, earthquake engineering, or manufacturing processes. To this end, it builds upon the combined theories of the gradient-enhanced continuum and the micropolar continuum. In the present paper, the theory is presented, strategies for its efficient implementation into a finite element framework are discussed, and realizations of the proposed framework by constitutive models for particular materials are developed. They are applied to finite element simulations of benchmark examples of cohesive-frictional material failure, and based on a comparison with experimental results from the literature, the proposed framework is assessed. The paper is organized as follows: in Section 2, the kinematic, kinetic and the constitutive relations of the framework are presented, and the numerical implementation of the continuum framework is discussed in Section 3. The stress update algorithm is presented in Section 4, highlighting in particular the return mapping algorithm. Sections 5 and 6 present realizations of the proposed framework for sandstone and concrete, and Section 7 concludes with a summary. Furthermore, in Appendix A an alternative to the decomposition of the wryness measure proposed in Section 2.3 is presented as an outlook to future research endeavors, and Appendices B and C contain the consistent tangent operators for the numerical implementation of the framework.

2. A finite strain gradient-enhanced micropolar framework for cohesive-frictional materials

While the focus of this work is concerned with an extended formulation of the micropolar continuum, in the following the kinematic relations, and the kinetic balance equations are introduced in the context of the more general micromorphic continuum of kinematic degree one and kinetic grade one, with the specialization to micropolar continuum presented subsequently. This is motivated by the employed elastic-plastic split, which is developed by departing from considerations at the micromorphic continuum, and furthermore, in view of a possible extension of the proposed framework to the more general micromorphic continuum in future, e.g., along the lines of the framework presented in [50, 90].

In the present work the notation used by Eringen [28] is adopted to the greatest extent. All relations are presented in the general curvilinear coordinate system G_I (undeformed configuration) and g_i (deformed configuration), making use of the index notation rather than the tensor notation due to the nonsymmetry of all involved tensors, implying summation over repeated indices. In this context, subscripts $(\bullet)_i$ and superscript $(\bullet)^i$ represent the co- and contravariant components of a quantity, $(\bullet)_{i,j}$ represents the covariant derivative, and $(\dot{\bullet}) = \frac{D(\bullet)}{Dt}$ designates the material time derivative of a tensor.

2.1. Kinematic relations

A micromorphic continuum in the sense of Eringen and Suhubi [30] is a continuous collection of deformable point particles, called macroelements. In particular, for a micromorphic continuum of kinematic degree one, each material particle is endowed with an additional triad of deformable directors, which describes the microscopic deformation. In addition to the classical macroscopic deformation gradient

$$F_I^i(t) = x^i_{,I}(t), \quad (1)$$

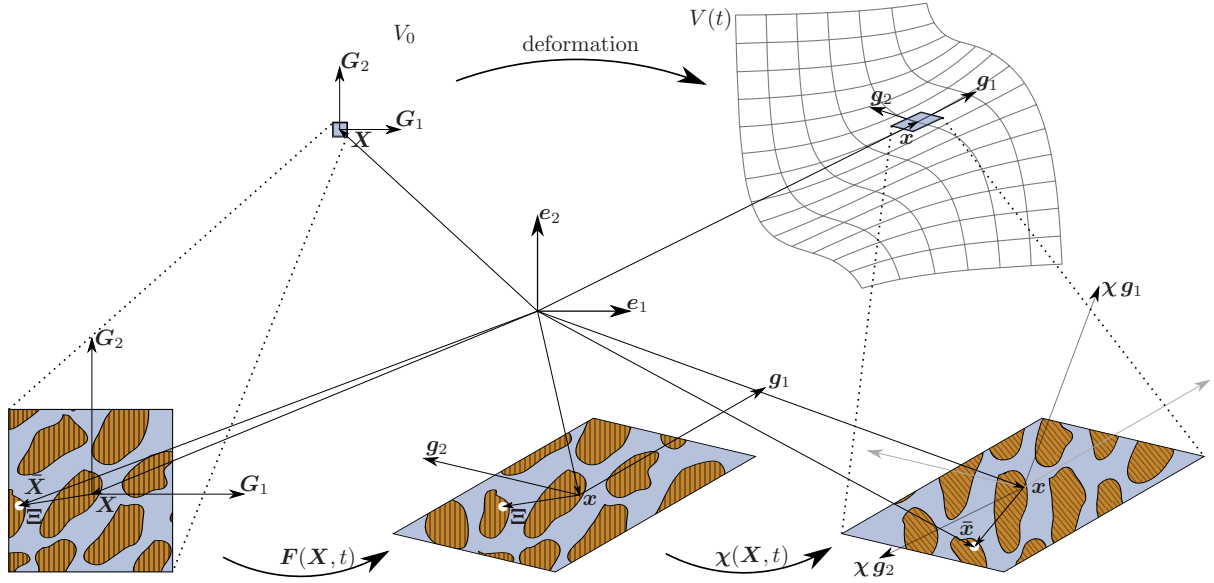


Figure 3: Illustration of the kinematics of Eringen's micromorphic continuum, considering the micropolar special case: The deformation state of a deformable material particle, i.e., a macroelement, is characterized by the macroscopic deformation gradient \mathbf{F} , indicated by the vectors $\mathbf{G}_1, \mathbf{G}_2$ (undeformed configuration) and $\mathbf{g}_1, \mathbf{g}_2$ (deformed configuration), and the microscopic deformation tensor χ , i.e., the microrotation within the macroelement, indicated by the orientation of the microelements (brown).

a microscopic deformation tensor $\chi_I^i(t)$ with its inverse $\mathfrak{X}_i^I(t)$

$$\mathfrak{X}_i^I(t) = (\chi^{-1}(t))^I_i \quad (2)$$

describes the microscopic deformation within a macroelement. Accordingly, the spatial position $\bar{x}^i(t)$ of a material point \bar{X}^i at time t , which is located within a macroelement with center of mass X^i , is determined by the spatial position of the macroelement $x^i(t)$ and the microdeformation tensor $\chi_I^i(t)$ within the macroelement by means of the affine transformation

$$\bar{x}^i(t) = x^i(t) + \chi_I^i(t) \Xi^I = x^i(t) + \xi^i(t) \quad (3)$$

with Ξ^I denoting the relative position of \bar{X}^i to X^I in the undeformed configuration V_0 , and with $\xi^i(t)$ denoting the relative position of $\bar{x}^i(t)$ to $x^i(t)$ in the deformed configuration $V(t)$ at time t . For the sake of readability, we omit an explicit declaration of a time dependency for all quantities in the following.

The micropolar continuum is considered a special case of the micromorphic continuum, for which the microscopic deformation is restricted to a rigid body rotation, cf. Figure 3. Thus, microdeformation tensor χ_I^i reduces to an orthogonal tensor with the property

$$\chi_I^i = G_{JI} \mathfrak{X}_j^J g^{ji}, \quad (4)$$

with G_{JI} and g^{ji} denoting the co- and contravariant coefficients of the metric tensors of the coordinate system in the undeformed and deformed configuration, respectively.

For characterizing the deformation state of a macroelement, it is useful to introduce a set of objective deformation tensors. Various sets have been proposed in the literature, see [28] for an overview. In the present work, a set of Lagrangian tensors, consisting of the deformation tensor

$$\mathfrak{C}_I^J = F_I^i \mathfrak{X}_i^J, \quad (5)$$

another microdeformation tensor

$$\mathcal{C}_{IJ} = \chi_I^i \chi_J^j g_{ij}, \quad (6)$$

and the wryness tensor

$$\Gamma_{LI}^K = \mathfrak{X}_i^K \chi_{L,I}^i \quad (7)$$

are employed.

For the special case of the micropolar continuum, Γ_{LI}^K is skew symmetric in the first two indices, and hence, an axial representation yields a simpler expression

$$\Gamma_{LI}^K = -\epsilon_{JML} \Gamma_I^J G^{KM} \quad (8)$$

with ϵ_{JML} denoting the Levi-Civita symbol of the general curvilinear coordinate system defined by its relation

$$\epsilon_{IJK} \sqrt{G}^{-1} = \varepsilon_{IJK} \quad (9)$$

to the Levi-Civita symbol of the Cartesian coordinate system ε_{IJK} , with $G = \det[G_{IJ}]$. Furthermore, for the micropolar continuum \mathcal{C}_{IJ} reduces to the identity tensor. For the micropolar continuum, \mathfrak{C}_I^J has the interesting property that it reduces to the classical Lagrangian stretch tensor in the case of coinciding macro- and microrotations. Hence, the rotational part of \mathfrak{C}_I^J is a measure of the difference between the macro- and microrotation.

For describing motions and thermodynamic considerations, Eulerian deformation rate measures are useful. Two particularly important measures are the spatial velocity gradient

$$l_j^i = \dot{F}_I^i F^{-1I}_j \quad (10)$$

and the spatial gyration rate

$$\nu_j^i = \dot{\chi}_I^i \mathfrak{X}_j^I. \quad (11)$$

For the micropolar continuum, skew symmetry $\nu_j^i = -\nu_j^i$ facilitates the axial representation by means of axial vector ν_k

$$\nu_j^i = -\epsilon^{ilk} \nu_k g_{lj} \quad (12)$$

with

$$\epsilon^{ijk} \sqrt{g} = \varepsilon^{ijk} \quad (13)$$

and $g = \det[g_{ij}]$.

For formulating the balance of power, the spatial deformation rate measures a_{ij} , b_{li}^k and c_{ij} are particularly useful, which are power conjugate to the Eulerian stress tensors introduced in Section 2.2 for

formulating the balance relations:

$$\begin{aligned} a_i^j &= l_i^j - \nu_i^j, \\ b_{li}^k &= \nu_{l,i}^k, \\ c_{ij} &= \frac{1}{2} (\nu_j^l g_{li} + \nu_i^l g_{lj}). \end{aligned} \quad (14)$$

Since for the micropolar continuum b_{li}^k and ν_j^i are skew symmetric, axial representation (12) facilitates the simpler representation $b_{li}^k = -\epsilon_j^k l_i^j$ with $\epsilon_j^k l_i^j = \epsilon_{jml} g^{km}$ and

$$b_i^j = \nu_{,i}^j, \quad (15)$$

and deformation rate c_{ij} vanishes identically.

Finally, it is trivial to show that those spatial deformation rates are related to the material time derivatives of the Lagrangian deformation tensors in (5), (6) and (7), i.e., $\dot{\mathbf{C}}_I^J$, $\dot{\Gamma}_{LI}^K$, and $\dot{\mathbf{C}}_{IJ}$, by push forward operations:

$$\begin{aligned} a_i^j &= \dot{\mathbf{C}}_I^J F^{-1I} \chi_i^J, \\ b_{li}^k &= \dot{\Gamma}_{LI}^K \chi_K^k \mathbf{x}_l^L F^{-1I} \chi_i^I, \\ c_{ij} &= \frac{1}{2} \dot{\mathbf{C}}_{IJ} \mathbf{x}_i^I \mathbf{x}_j^J, \end{aligned} \quad (16)$$

and for the special case of the micropolar continuum

$$\begin{aligned} b_i^j &= \dot{\Gamma}_I^J \chi_i^J F^{-1I} \chi_i^I, \\ c_{ij} &= 0. \end{aligned} \quad (17)$$

2.2. Balance relations

The three kinetic balance equations for the proposed gradient-enhanced micropolar framework consist of the two balance equations of the micropolar continuum theory, and the balance equation describing the nonlocal character of material damage. The balance equations of the micropolar continuum follow as a special case of the balance relations of the micromorphic continuum, which can be derived by means of a spatial averaging procedure [26, 30], see also [37], by means of the principle of virtual work [36], by means of the requirement of invariance of the balance of energy under the Galilean group of transformations [27], or by statistical mechanics [76]. The resulting kinetic balance equations of the general micromorphic continuum of degree one are formed by the balance of linear momentum

$$t_{j,i}^i + \rho(f_j - \ddot{x}_j) = 0 \quad \text{in } V(t), \quad (18)$$

and the balance of momentum moments

$$m_{k,i}^{i,l} + t_k^l - s_k^l + \rho(l_k^l - \sigma_k^l) = 0 \quad \text{in } V(t). \quad (19)$$

Tensors t_j^i , s_j^i , $m_k^{i,l}$, designate the macroscopic, in general nonsymmetric Cauchy stress tensor, the symmetric micro stress tensor, and the nonsymmetric couple stress tensor, respectively. Furthermore, ρ designates the mass density, f_j the body force per unit mass, l_k^l the body couple per unit mass, and σ_k^l the micro spin inertia per unit mass.

For the micropolar continuum, the couple stress tensor m_k is skew symmetric in the last two indices, and hence, the axial representation

$$m_k^{i\ l} = -\frac{1}{2}\epsilon_k^{j\ l} m_j^i \quad (20)$$

with m_j^i denoting the micropolar couple stress, and with shorthand $\epsilon_k^{j\ l} = \epsilon^{jml} g_{mk}$ allows to express the balance of momentum moments by means of the reduced, well known balance of angular momentum of the micropolar continuum

$$m_{j,i}^i + \epsilon_{jk}^l t_l^k + \rho(l_j - \sigma_j) = 0 \quad \text{in } V(t) \quad (21)$$

with l_j denoting the body torque density per unit mass and σ_j denoting the micro rotatory inertia. Furthermore,

$$\frac{1}{2}(t^{ij} + t^{ji}) = s^{ij} \quad (22)$$

holds.

The third kinetic balance equation of the proposed gradient-enhanced micropolar framework is formed by the balance equation of the continuum enhanced by gradients of internal variables, expressed by means of the second order partial differential equation

$$\tilde{\alpha} - l_d^2 (\tilde{\alpha}_{,I})_{,J} G^{IJ} = \alpha_d \quad \text{in } V_0, \quad (23)$$

commonly denoted as the *Helmholtz-like* equation. It describes the nonlocal character of material damage in terms of the independent, damage driving quantity $\tilde{\alpha}$, as originally proposed by Peerlings et al. [80]. Note that this balance relation is defined completely in the undeformed configuration, i.e., derivatives are taken with respect to material coordinates rather than spatial coordinates, and balance is formulated in the undeformed body V_0 . This is motivated by physical considerations, as discussed in [99]. Therein, it is concluded that only a Lagrangian formulation yields the desired regularizing properties, whereas Eulerian or mixed Eulerian-Lagrangian formulations may lead to physically implausible results. Equation (23) is widely used and has been employed successfully for describing the nonlocal character of damage of various materials, in particular in the small strain regime. It has been presented in [80] in an ad hoc fashion, making no considerations regarding a thermodynamic balance relation. For the purpose of thermodynamic considerations it is recast in the spirit of [32] into the form

$$(\eta^I)_{,I} - \zeta = 0 \quad \text{in } V_0, \quad (24)$$

with η^I and ζ denoting the thermodynamic forces, denoted as generalized stresses by Forest [32], which are conjugate to $\tilde{\alpha}_{,I}$ and $\tilde{\alpha}$, respectively. The relation of those forces to the nonlocal damage driving field $\tilde{\alpha}$ and its material gradient $\tilde{\alpha}_{,I}$ will be established in Section 2.4 by means of constitutive relations.

The internal power per undeformed volume \dot{E} of the combined micropolar continuum and the gradient-enhanced continuum, restricting the discussion to the isothermal process for the sake of simplicity, then consists of the stress power, the couple stress power and the power related to the nonlocal material damage process

$$\dot{E} = J t_j^i a_i^j + J m_j^i b_j^i + \zeta \dot{\tilde{\alpha}} + \eta^I \dot{\tilde{\alpha}}_{,I} \quad \text{in } V_0. \quad (25)$$

Therein, J denotes the determinant of the macroscopic deformation gradient F^i_I , which relates an in-

finitesimal volume element of the undeformed configuration dV_0 to the one in the deformed configuration $dV(t)$ as

$$J = \frac{dV(t)}{dV_0}. \quad (26)$$

After introducing a suitable elastic-plastic split of the kinematic variables, (25) will be used for formulating the dissipation inequality, and for deriving the general form of the constitutive relations.

2.3. Elastic-plastic split in the micropolar continuum

For formulating plastic material behavior within the geometrically exact micropolar continuum theory, basically two schools emerged in the past 20 years: They are the approach (i) first proposed by Steinmann [98], adopted by Bauer et al. [5], Grammenoudis and Tsakmakis [38], Johannsen and Tsakmakis [55, 56], and the approach (ii) developed independently by Dłuzewski [20], Forest et al. [34], Sansour [92], Sievert et al. [96].

For representing inelastic material behavior at the macroscopic level, for both approaches (i) and (ii) a multiplicative decomposition of the macroscopic deformation gradient is assumed. However at the microscopic level, Steinmann [98] similarly assumes a multiplicative decomposition of the microdeformation tensor for approach (i), whereas Dłuzewski [20], Forest et al. [34], Sansour [92], Sievert et al. [96] directly assume an additive decomposition of a Lagrangian wryness measure for their approach (ii).

Departing from considerations in the context of the general micromorphic continuum, we follow here approach (ii), employing an additive decomposition of the wryness tensor. Accordingly, at the macroscopic level, an elastic-plastic split based on the multiplicative decomposition of the deformation gradient F_I^i is introduced as

$$F_I^i = F_{\bar{K}}^{ei} F^{p\bar{K}}_I, \quad (27)$$

commonly known as the Kröner-Lee decomposition.

Since for the micropolar continuum the microdeformation is restricted to a rigid body rotation, the microdeformation tensor \mathcal{C}_{IJ} , the microdeformation rate c_{ij} , and the internal power related to micro stress s^{ij} vanish identically. Accordingly, no dissipation is associated with the microscopic deformation within a single macroelement, i.e., at the microscopic level. From a physical point of view, since no stress measure is associated with the dissipative mechanism, a decomposition of the microscopic deformation into elastic and plastic part seems unmotivated. Sansour [92] argues in a similar way, stating that the field of microrotations is considered an independent kinematic variable, which is not amenable to a decomposition into elastic and plastic parts, similar to the displacement field.

On the other hand, as apparent in (25), the micropolar couple stress power is in general nonzero, and dissipative effects related to the gradient of the microdeformation field may occur. Hence it is implied that for the micropolar continuum plastic material behavior does not occur within a macroelement, but rather in between neighboring macroelements, and consequently, inelastic material behavior is observed in the gradient of the microdeformation field.

For the proposed approach, this is expressed by means of an additive decomposition of the material gradient $\chi^i_{J,K}$:

$$\chi^i_{J,K} = \chi^{ei}_{J,K} + \chi^{pi}_{J,K}. \quad (28)$$

By means of this additive decomposition no fictitious, i.e., elastically unloaded, intermediate configuration

is introduced at the microscopic level within a macroelement, which is in sharp contrast to approach (i) proposed in [98].

Using multiplicative decomposition (27), the elastic deformation tensor $\mathfrak{C}_{\bar{I}}^{eJ}$ is introduced, which is computed by means of the multiplicative decomposition

$$\mathfrak{C}_{\bar{I}}^{eJ} = F^{ei} \mathfrak{X}_i^J = (F^p)^{-1\bar{I}} \mathfrak{C}_{\bar{I}}^J. \quad (29)$$

For the wryness tensor Γ_{LI}^K , the assumed additive elastic-plastic split of $\chi_{J,K}^i$ results in the additive elastic-plastic split

$$\Gamma_{LI}^K = \Gamma_{LI}^{eK} + \Gamma_{LI}^{pK}, \quad (30)$$

with the respective elastic and plastic parts defined as

$$\begin{aligned} \Gamma_{LI}^{eK} &= \mathfrak{X}_i^K \chi_{L,I}^{ei}, \\ \Gamma_{LI}^{pK} &= \mathfrak{X}_i^K \chi_{L,I}^{pi}. \end{aligned} \quad (31)$$

The material time derivatives follow accordingly as

$$\dot{\Gamma}_{LI}^K = -\mathfrak{X}_{k,J}^K \dot{\chi}_{L,I}^k \mathfrak{X}_i^J \chi_{L,I}^i + \mathfrak{X}_{k,L}^K \dot{\chi}_{L,I}^k = \dot{\Gamma}_{LI}^{eK} + \dot{\Gamma}_{LI}^{pK}, \quad (32)$$

with

$$\begin{aligned} \dot{\Gamma}_{LI}^{eK} &= -\mathfrak{X}_{k,J}^K \dot{\chi}_{L,I}^k \mathfrak{X}_i^J \chi_{L,I}^{ei} + \mathfrak{X}_{i,L}^K \dot{\chi}_{L,I}^{ei}, \\ \dot{\Gamma}_{LI}^{pK} &= -\mathfrak{X}_{k,J}^K \dot{\chi}_{L,I}^k \mathfrak{X}_i^J \chi_{L,I}^{pi} + \mathfrak{X}_{i,L}^K \dot{\chi}_{L,I}^{pi}. \end{aligned} \quad (33)$$

For the micropolar continuum, the simplified relations read

$$\Gamma_I^J = \Gamma_I^{eJ} + \Gamma_I^{pJ} \quad (34)$$

with

$$\begin{aligned} \Gamma_I^{eJ} &= -\frac{1}{2} \epsilon_{K}^J \epsilon_{L}^L \mathfrak{X}_k^K \chi_{L,I}^{ek}, \\ \Gamma_I^{pJ} &= -\frac{1}{2} \epsilon_{K}^J \epsilon_{L}^L \mathfrak{X}_k^K \chi_{L,I}^{pk}. \end{aligned} \quad (35)$$

using shorthand $\epsilon_K^J \epsilon_L^L = \epsilon^{JML} G_{MK}$. The material time derivatives follow as

$$\dot{\Gamma}_I^J = \dot{\Gamma}_I^{eJ} + \dot{\Gamma}_I^{pJ} \quad (36)$$

with

$$\begin{aligned} \dot{\Gamma}_I^{eJ} &= -\frac{1}{2} \epsilon_{K}^J \epsilon_{L}^L \left(\dot{\mathfrak{X}}_i^K \chi_{L,I}^{ei} + \mathfrak{X}_{i,L}^K \dot{\chi}_{L,I}^{ei} \right), \\ \dot{\Gamma}_I^{pJ} &= -\frac{1}{2} \epsilon_{K}^J \epsilon_{L}^L \left(\dot{\mathfrak{X}}_i^K \chi_{L,I}^{pi} + \mathfrak{X}_{i,L}^K \dot{\chi}_{L,I}^{pi} \right). \end{aligned} \quad (37)$$

Accordingly, it is concluded that the additive elastic-plastic split of the material gradient of the microdeformation field results in an additive decomposition of the wryness tensors and its material time derivatives. Such an additive decomposition of the wryness tensors was assumed in an ad hoc fashion by Sansour [92], and it follows naturally from assumption (28).

The proposed elastic-plastic split for the material gradient of the microdeformation assumes that the elastic part is defined with respect to the undeformed macroscopic configuration rather than the macroscopic stress free intermediate configuration. In this regard, the resulting elastic wryness tensor is in line with the approach (i) by Steinmann [98], but it is in contrast to the approach (ii) by Dłuzewski [20], Forest et al. [34], Sievert et al. [96]. For the latter approach, the elastic wryness tensor is defined with respect to the macroscopic stress free intermediate configuration. This way, mixed reference configurations of the variables of the free energy function could be avoided. A recent discussion on the choice of variables was also presented by Forest [33].

Remark: A formulation for the additive elastic-plastic split presented herein defined with respect to the macroscopic stress free intermediate configuration, in line with approach (ii) by Dłuzewski [20], Forest et al. [34], Sievert et al. [96], could be stated as

$$\chi^i_{L,I} = (\chi^{ei}_{L,\bar{I}} + \chi^{pi}_{L,\bar{I}}) F^{p\bar{I}}_I, \quad (38)$$

with $\chi^{ei}_{L,\bar{I}}$ denoting the elastic part. While the present work focuses on the decomposition (28), a concise outline of decomposition (38) is presented together with the thermodynamic implications in Appendix A. For the presented realizations of the gradient-enhanced micropolar continuum framework in Sections 5 and 6, the obtained results are in good agreement with experimental results, and the presented approach is thermodynamically consistent. Clearly, which of both approaches is in better agreement with reality depends on the material, and the micromechanics processes associated with inelastic material behavior of such a material. Such investigations remain to be performed in the future.

Employing the elastic-plastic splits (27) and (28), the deformation rate tensors are now reformulated. As known from the classical Boltzmann continuum, the Kröner-Lee decomposition (27) results in an additive split of the spatial velocity gradient

$$\begin{aligned} l^i_j &= \dot{F}^i_K F^{-1K}_j \\ &= \left(\dot{F}^{ei}_{\bar{I}} F^{p\bar{I}}_K + F^{ei}_{\bar{I}} \dot{F}^{p\bar{I}}_K \right) (F^p)^{-1K}_{\bar{J}} (F^e)^{-1\bar{J}}_j \\ &= l^{ei}_j + F^{ei}_{\bar{I}} L^{p\bar{I}}_{\bar{J}} (F^e)^{-1\bar{J}}_j, \end{aligned} \quad (39)$$

in which l^{ei}_j denotes the elastic velocity gradient, defined with respect to the deformed configuration as

$$l^{ei}_j = \dot{F}^{ei}_{\bar{K}} (F^e)^{-1\bar{K}}_j \quad (40)$$

and $L^{p\bar{I}}_{\bar{J}}$ denotes the plastic velocity gradient, which is defined completely with respect to the plastic intermediate configuration as

$$L^{p\bar{I}}_{\bar{J}} = \dot{F}^{p\bar{I}}_K (F^p)^{-1K}_{\bar{J}}. \quad (41)$$

Similarly, the spatial deformation rate tensor a_i decomposes as

$$\begin{aligned}
a_i^j &= l_i^j - \dot{\chi}_I^j \mathfrak{X}_i^I \\
&= \left(\dot{F}_{\bar{I}}^{eJ} (F^e)^{-1\bar{I}}_i - \dot{\chi}_I^j \mathfrak{X}_i^I \right) + F^{eJ}_{\bar{J}} L^{p\bar{J}}_{\bar{I}} (F^e)^{-1\bar{I}}_i \\
&= \dot{\mathfrak{C}}_{\bar{I}}^{eJ} (F^e)^{-1\bar{I}}_i \chi^j_J + F^{eJ}_{\bar{J}} L^{p\bar{J}}_{\bar{I}} (F^e)^{-1\bar{I}}_i
\end{aligned} \tag{42}$$

with

$$\dot{\mathfrak{C}}_{\bar{I}}^{eJ} = \dot{F}^{e^i}_{\bar{I}} \mathfrak{X}_i^J - F^{e^i}_{\bar{I}} \mathfrak{X}_j^J \dot{\chi}_K^j \mathfrak{X}_i^K. \tag{43}$$

For the special case of the micropolar continuum, this simplifies to

$$\dot{\mathfrak{C}}_{\bar{I}}^{eJ} = \dot{F}^{e^i}_{\bar{I}} \mathfrak{X}_i^J + F^{e^i}_{\bar{I}} \dot{\mathfrak{X}}_i^J. \tag{44}$$

Observe that in contrast to the macroscopic spatial velocity gradient l_i^j , the spatial gyration rate ν_i^j is not affected by the introduced split of the gradient of the microdeformation tensor, as apparent from (11). By contrast, for the spatial deformation rate tensor b_{li}^k , an additive split results as

$$\begin{aligned}
b_{li}^k &= \nu_{li}^k \\
&= \dot{\Gamma}_{LI}^K F^{-1I}_i \mathfrak{X}_l^L \chi_K^k \\
&= \left(\dot{\Gamma}_{LI}^{eK} + \dot{\Gamma}_{LI}^{pK} \right) F^{-1I}_i \mathfrak{X}_l^L \chi_K^k
\end{aligned} \tag{45}$$

which simplifies for the micropolar continuum to

$$b_i^j = \left(\dot{\Gamma}_I^{eJ} + \dot{\Gamma}_I^{pJ} \right) F^{-1I}_i \chi^j_J \tag{46}$$

Hence, the proposed additive split of the gradient of microdeformation results in an additive split of the deformation rate tensor b_i^j .

2.4. Dissipation inequality and general constitutive relations

By means of the Clausius-Duhem (C-D) inequality, the dissipative mechanisms related to the proposed elastic-plastic split are inspected. The dissipation inequality is established from the difference between the rate of the Helmholtz free energy density Ψ and the internal power per undeformed volume \dot{E} as

$$\mathcal{D} = \dot{E} - \rho_0 \dot{\Psi} \geq 0 \quad \text{in } V_0, \tag{47}$$

with \mathcal{D} denoting the dissipation rate per undeformed volume. Taking (25), the inequality is expanded for the gradient-enhanced micropolar framework as

$$-\rho_0 \dot{\Psi} + J t^i_j a_i^j + J m^i_j b_i^j + \zeta \dot{\tilde{\alpha}} + \eta^I \dot{\tilde{\alpha}}_{,I} \geq 0 \quad \text{in } V_0. \tag{48}$$

For the proposed gradient-enhanced micropolar damage-plasticity framework, the Helmholtz free energy density Ψ is assumed a function of the elastic deformation tensor $\mathfrak{C}_{\bar{I}}^{eJ}$, the elastic wryness tensor $\Gamma_{\bar{I}}^{eJ}$, the nonlocal damage driving field $\tilde{\alpha}$ and its material gradient $\tilde{\alpha}_{,I}$, a scalar isotropic material damage

parameter $0 \leq \omega \leq 1$, and a set of internal state variables α^\bullet :

$$\Psi = \Psi(\mathfrak{C}_{\bar{I}}^{eJ}, \Gamma_{I}^{eJ}, \tilde{\alpha}, \tilde{\alpha}_{,I}, \omega, \alpha^\bullet). \quad (49)$$

The set of internal state variables α^\bullet represents the history of the material, e.g., the hardening state, expressed by tensor quantities of arbitrary order.

Strictly speaking, the damage parameter ω is nothing else than an internal state variable, but in order to highlight the concept of continuum damage mechanics within the proposed framework, it is considered explicitly in the following derivations.

From (49), the rate of the Helmholtz free energy density follows as

$$\dot{\Psi} = \frac{\partial \Psi}{\partial \mathfrak{C}_{\bar{I}}^{eJ}} \dot{\mathfrak{C}}_{\bar{I}}^{eJ} + \frac{\partial \Psi}{\partial \Gamma_{I}^{eJ}} \dot{\Gamma}_{I}^{eJ} + \frac{\partial \Psi}{\partial \tilde{\alpha}} \dot{\tilde{\alpha}} + \frac{\partial \Psi}{\partial \tilde{\alpha}_{,I}} \dot{\tilde{\alpha}}_{,I} + \frac{\partial \Psi}{\partial \omega} \dot{\omega} + \frac{\partial \Psi}{\partial \alpha^\bullet} \dot{\alpha}^\bullet, \quad (50)$$

which allows to rewrite the C-D inequality as

$$\begin{aligned} -\rho_0 \left(\frac{\partial \Psi}{\partial \mathfrak{C}_{\bar{I}}^{eJ}} \dot{\mathfrak{C}}_{\bar{I}}^{eJ} + \frac{\partial \Psi}{\partial \Gamma_{I}^{eJ}} \dot{\Gamma}_{I}^{eJ} + \frac{\partial \Psi}{\partial \tilde{\alpha}} \dot{\tilde{\alpha}} + \frac{\partial \Psi}{\partial \tilde{\alpha}_{,I}} \dot{\tilde{\alpha}}_{,I} + \frac{\partial \Psi}{\partial \omega} \dot{\omega} + \frac{\partial \Psi}{\partial \alpha^\bullet} \dot{\alpha}^\bullet \right) \\ + J t_j^i a_i^j + J m_j^i b_j^i + \dot{\tilde{\alpha}} \zeta + \dot{\tilde{\alpha}}_{,I} \eta^I \geq 0 \quad \text{in } V_0. \end{aligned} \quad (51)$$

Therein, the term $J t_j^i a_i^j$ represents the rate of the work produced by the Cauchy stress per reference volume dV_0

$$\begin{aligned} J t_j^i a_i^j &= J t_j^i (l_j^i - \nu_j^i) \\ &= J t_j^i \left(\dot{F}_{K}^j F^{-1K}_i - \dot{\chi}_{K}^j \mathfrak{X}_{iK}^K \right) \\ &= J t_j^i \left(\dot{F}_{\bar{I}}^{eJ} (F^e)^{-1\bar{I}}_i - \dot{\chi}_{K}^j \mathfrak{X}_{iK}^K \right) + J t_j^i \left(F^{ej}_j L^{p\bar{J}}_{\bar{I}} (F^e)^{-1\bar{I}}_i \right), \end{aligned} \quad (52)$$

which, using (44) and (41), is rewritten as

$$J t_j^i a_i^j = T_{\bar{I}}^{\bar{I}} \dot{\mathfrak{C}}_{\bar{I}}^{eJ} + \mathcal{T}_{\bar{I}}^{\bar{I}} L^{p\bar{J}}_{\bar{I}}. \quad (53)$$

Therein, the Biot stress measure $T_{\bar{I}}^{\bar{I}}$, which is power conjugate to the elastic Cosserat deformation rate $\dot{\mathfrak{C}}_{\bar{I}}^{eJ}$, is defined with respect to both the undeformed and the stress free intermediate configurations, and it is expressed as

$$T_{\bar{I}}^{\bar{I}} = J (F^e)^{-1\bar{I}}_i t_j^i \chi_{\bar{I}}^j, \quad (54)$$

and the Mandel stress measure $\mathcal{T}_{\bar{I}}^{\bar{I}}$, which is power conjugate to the plastic velocity gradient $L^{p\bar{J}}_{\bar{I}}$, is defined in the intermediate configuration as

$$\mathcal{T}_{\bar{I}}^{\bar{I}} = J (F^e)^{-1\bar{I}}_i t_j^i F^{ej}_{\bar{I}}. \quad (55)$$

The term $J m_j^i b_j^i$ in (48), represents the couple stress power per reference volume dV_0 , which is now expanded as

$$\begin{aligned} J m_j^i b_j^i &= J m_j^i F^{-1I}_i \chi_{J}^j \left(\dot{\Gamma}_{I}^{eJ} + \dot{\Gamma}_{I}^{pJ} \right) \\ &= M_{J}^I \left(\dot{\Gamma}_{I}^{eJ} + \dot{\Gamma}_{I}^{pJ} \right) \end{aligned} \quad (56)$$

with the Biot couple stress tensor $M_{\bar{J}}$ defined as

$$M_{\bar{J}}^I = J m_j^i F^{-1I}{}_i \chi^j_{\bar{J}}. \quad (57)$$

Combining (51), (53) and (56) and rearranging results in

$$\begin{aligned} \left(T_{\bar{J}}^{\bar{I}} - \rho_0 \frac{\partial \Psi}{\partial \mathfrak{C}_{\bar{I}}^e{}^{\bar{J}}} \right) \dot{\mathfrak{C}}_{\bar{I}}^e{}^{\bar{J}} + \left(M_{\bar{J}}^I - \rho_0 \frac{\partial \Psi}{\partial \Gamma^e{}^{\bar{J}}{}_I} \right) \dot{\Gamma}^e{}^{\bar{J}}{}_I + \left(\zeta - \rho_0 \frac{\partial \Psi}{\partial \tilde{\alpha}} \right) \dot{\tilde{\alpha}} + \left(\eta^I - \rho_0 \frac{\partial \Psi}{\partial \tilde{\alpha}_{,I}} \right) \dot{\tilde{\alpha}}_{,I} \\ + \mathcal{T}_{\bar{J}}^{\bar{I}} L^{\text{p}\bar{J}}_{\bar{I}} + M_{\bar{J}}^I \dot{\Gamma}^{\text{p}\bar{J}}{}_I + Y \dot{\omega} - \beta_{\bullet} \dot{\alpha}^{\bullet} \geq 0 \quad \text{in } V_0, \end{aligned} \quad (58)$$

in which

$$Y = -\rho_0 \frac{\partial \Psi}{\partial \omega} \quad (59)$$

is commonly denoted as the energy release rate and

$$\beta_{\bullet} = \rho_0 \frac{\partial \Psi}{\partial \alpha^{\bullet}} \quad (60)$$

denotes the quasi-conservative thermodynamic force conjugate to the internal state variable α^{\bullet} .

The Coleman-Noll procedure [13] is then applied, requiring that non-negative dissipation must be fulfilled for arbitrary, independent rate processes, and accordingly, the terms in parentheses must vanish identically, resulting in the constitutive relations

$$T_{\bar{J}}^{\bar{I}} = \rho_0 \frac{\partial \Psi}{\partial \mathfrak{C}_{\bar{I}}^e{}^{\bar{J}}}, \quad M_{\bar{J}}^I = \rho_0 \frac{\partial \Psi}{\partial \Gamma^e{}^{\bar{J}}{}_I}, \quad \zeta = \rho_0 \frac{\partial \Psi}{\partial \tilde{\alpha}}, \quad \eta^I = \rho_0 \frac{\partial \Psi}{\partial \tilde{\alpha}_{,I}} \quad (61)$$

yielding the final simplified dissipation inequality

$$\mathcal{T}_{\bar{J}}^{\bar{I}} L^{\text{p}\bar{J}}_{\bar{I}} + M_{\bar{J}}^I \dot{\Gamma}^{\text{p}\bar{J}}{}_I + Y \dot{\omega} - \beta_{\bullet} \dot{\alpha}^{\bullet} \geq 0 \quad \text{in } V_0. \quad (62)$$

2.5. Free energy potential

Further specialization of the free energy potential is performed to introduce continuum damage into the constitutive relations, and for relating the thermodynamic forces ζ and η^I to the nonlocal damage driving field $\tilde{\alpha}$ in (24).

To this end, an additive structure of the free energy per unit mass Ψ

$$\rho_0 \Psi = \rho_0 \left(\Psi^e(\mathfrak{C}_{\bar{I}}^e{}^{\bar{J}}, \Gamma^e{}^{\bar{J}}{}_I, \omega) + \Psi^{\text{p}}(\alpha^{\bullet}, \omega) + \tilde{\Psi}(\tilde{\alpha}, \tilde{\alpha}_{,I}) \right) \quad (63)$$

is considered, explicitly employing damage parameter ω for representing the degradation of the stress, couple stress and hardening thermodynamic forces, or parts thereof by reducing partially or completely the elastic free energy potential $\Psi^e(\mathfrak{C}_{\bar{I}}^e{}^{\bar{J}}, \Gamma^e{}^{\bar{J}}{}_I)$ and the hardening free energy potential $\Psi^{\text{p}}(\alpha^{\bullet})$, and with $\tilde{\Psi}(\tilde{\alpha}, \tilde{\alpha}_{,I})$ denoting the complementary part for the gradient-enhanced formulation. Relation (63) represents the simplest setting for considering a dependency of the elastic properties on continuum damage. More refined constitutive laws can be formulated in the same manner, e.g., considering multiple or higher order damage tensors. Accordingly, stress measures t_j^i and m_j^i follow from (63) by means of the hyperelastic

relations

$$t_j^i = J^{-1} F^{ei} \bar{\mathbf{x}}_j^J \rho_0 \frac{\partial \Psi^e(\mathbf{c}_{\bar{I}}^e, \Gamma_{I}^e, \omega)}{\partial \mathbf{c}_{\bar{I}}^e}, \quad m_j^i = J^{-1} F_I^i \bar{\mathbf{x}}_j^J \rho_0 \frac{\partial \Psi^e(\mathbf{c}_{\bar{I}}^e, \Gamma_{I}^e, \omega)}{\partial \Gamma_{I}^e}. \quad (64)$$

Furthermore, assuming

$$\rho_0 \tilde{\Psi}(\tilde{\alpha}, \tilde{\alpha}_{,I}, \alpha_d) = \frac{1}{2} (l_d)^2 \tilde{\alpha}_{,I} G^{IJ} \tilde{\alpha}_{,J} + \frac{1}{2} (\alpha_d - \tilde{\alpha})^2 \quad (65)$$

for the complementary part yields equivalence of (24) with the well known classical form (23). The latter is considered in the remainder of this work.

2.6. Plasticity part

The evolution of the plastic deformation gradient $F^{\bar{I}}$ and the plastic wryness $\Gamma^{\bar{I}}$, as well as the set of internal state variables α^\bullet are described by means of a yield condition, a flow rule and a hardening rule. For the sake of simplicity, it is assumed that the set of internal state variables α^\bullet is related to the plasticity part of the model, i.e., the evolution of α^\bullet is linked to plastic flow. A generalization for representing non-plasticity related internal state variables, e.g., for modeling creep, is straightforward, and hence, it is not considered further in the present contribution.

In case of combined continuum damage mechanics and plasticity theory, the question arises whether plasticity is formulated in the nominal stress space, i.e., by means of $\bar{T}^{\bar{I}}, \bar{M}^{\bar{I}}, \bar{\beta}_\bullet$ (or any stress measure derived thereof), or in the effective stress space

$$\bar{T}^{\bar{I}}_J = \rho_0 \left. \frac{\partial \Psi}{\partial \mathbf{c}_{\bar{I}}^e} \right|_{\omega=0}, \quad \bar{M}^{\bar{I}}_J = \rho_0 \left. \frac{\partial \Psi}{\partial \Gamma_{I}^e} \right|_{\omega=0}, \quad \bar{\beta}_\bullet = \rho_0 \left. \frac{\partial \Psi}{\partial \alpha^\bullet} \right|_{\omega=0} \quad (66)$$

interpreted as *forces per intact area of the material*. A discussion on this question is found in [40]. Therein, it is concluded that the formulation in the nominal stress space is subjected to severe restrictions in order to ensure a unique model response. Hence, a formulation in the effective stress space is employed for the proposed framework.

The concept of generalized stress invariants [15, 68, 74, 101], computed from both the effective stress tensor and the effective couple stress tensor, allows to employ the classical framework of plasticity in terms of a single, combined yield function for both stress tensors, initially proposed by Lippmann [65]. Then, in the spirit of non-associated finite strain plasticity, a yield function $f_p(\bar{T}^{\bar{I}}, \bar{M}^{\bar{I}}, \bar{\beta}_\bullet)$ is employed for delimiting the elastic domain, together with the Karush-Kuhn-Tucker conditions of optimization

$$f_p(\bar{T}^{\bar{I}}, \bar{M}^{\bar{I}}, \bar{\beta}_\bullet) \leq 0, \quad \dot{\lambda} \geq 0, \quad \dot{\lambda} f(\bar{T}^{\bar{I}}, \bar{M}^{\bar{I}}, \bar{\beta}_\bullet) = 0. \quad (67)$$

For non-associated plasticity, a plastic potential function $g_p(\bar{T}^{\bar{I}}, \bar{M}^{\bar{I}}, \bar{\beta}_\bullet)$, and a hardening potential function $h_p(\bar{T}^{\bar{I}}, \bar{M}^{\bar{I}}, \bar{\beta}_\bullet)$, which, in general, are different from $f_p(\bar{T}^{\bar{I}}, \bar{M}^{\bar{I}}, \bar{\beta}_\bullet)$, are used for describing the evolution of the thermodynamically conjugate quantities as

$$L^{\bar{p}\bar{I}} = \dot{\lambda} \frac{\partial g_p(\bar{T}^{\bar{I}}, \bar{M}^{\bar{I}}, \bar{\beta}_\bullet)}{\partial \bar{T}^{\bar{I}}_J}, \quad \Gamma^{\bar{p}\bar{I}} = \dot{\lambda} \frac{\partial g_p(\bar{T}^{\bar{I}}, \bar{M}^{\bar{I}}, \bar{\beta}_\bullet)}{\partial \bar{M}^{\bar{I}}_J}, \quad \dot{\alpha}^\bullet = -\dot{\lambda} \frac{\partial h_p(\bar{T}^{\bar{I}}, \bar{M}^{\bar{I}}, \bar{\beta}_\bullet)}{\partial \bar{\beta}_\bullet}. \quad (68)$$

Such non-associated plastic potential functions are in particular important for cohesive-frictional materials,

for which associated flow rules would yield an overestimation of the volumetric plastic flow. Extension of the presented framework to multisurface plasticity by means of Koiter's [58] generalized flow rule are straightforward, and hence, a detailed explanation is omitted here.

Remark: As a consequence of the employed elastic-plastic split, i.e., the assumption that plastic behavior occurs in the gradient of the microdeformation rather than introducing a multiplicative decomposition of the microdeformation itself, the proposed framework is equivalent to the framework proposed in [74] in case of infinitesimal deformations.

2.7. Damage part

Following the thermodynamic approach to constitutive modeling, a dissipation potential $g_d(Y, T^I_J, M^I_J, \alpha_d, \tilde{\alpha}, \beta_\bullet)$ may be used for describing the evolution of damage as

$$\dot{\omega} = \frac{\partial g_d(Y, T^I_J, M^I_J, \alpha_d, \tilde{\alpha}, \beta_\bullet)}{\partial Y}, \quad (69)$$

e.g., formulated in terms of a threshold function for a critical value of the energy release rate, similar to classical plasticity theory. However, for cohesive-frictional materials with highly nonlinear material behavior, such dissipation potentials may be difficult or even impossible to formulate, and hence, commonly rate type evolution laws are formulated directly. Accordingly, for the proposed framework the latter approach is pursued, and the damage evolution is assumed to depend on the nonlocal damage driving field through

$$\dot{\omega} = \dot{\omega}(\dot{\tilde{\alpha}}). \quad (70)$$

To ensure non-negative dissipation in (62) for non-healing materials the restriction $\dot{\omega} \geq 0$ is sufficient considering that the energy release rate Y is always non-negative.

Alternative approaches, assuming a dependency on both $\tilde{\alpha}$ and α_d are reported in the literature. In particular so-called over-nonlocal approaches [18] are widely used. Since the extension to such a formulation is straightforward, it is not considered further in the present contribution.

Similar to (70), a rate type evolution law in lieu of a dissipation potential may be used for describing the evolution of α_d . For combined damage-plasticity approaches, the evolution of damage driving variable α_d is commonly related to the evolution of plastic deformation

$$\dot{\alpha}_d = \dot{\alpha}_d(\dot{F}^p_I, \dot{\Gamma}^p_J, \dot{\alpha}_\bullet, t^i_j, m^i_j, \beta_\bullet) \quad (71)$$

with a potential dependency on the stress state to account for ductile and brittle behavior in compression and tension, respectively, and with the restriction

$$\dot{\alpha}_d \geq 0 \quad (72)$$

for ensuring a monotonic growth of damage.

3. Nonlinear finite element implementation of the gradient-enhanced micropolar continuum

For numerical implementation of the proposed framework by means of the finite element method, the spatially discretized weak forms of the governing second order partial differential equations (18), (19), and

(23) are formulated. For the sake of simplicity, the quasi-static case is considered, i.e., inertial terms in the balance equations are neglected, no body forces or body couples are considered, and furthermore, homogeneous Neumann boundary conditions are assumed for (21) and (23). For representing finite micropolar rotations in a computational framework, a three parameter representation in terms of the axial vector w_i and the Euler-Rodrigues formula

$$\chi^i_I = \cos(w) g^i_I - \sin(w) \epsilon^{ijk} n_k g_{jI} + (1 - \cos(w)) n^i n_j g^j_I \quad (73)$$

with

$$n_i = w_i/w \quad \text{and} \quad w = \sqrt{w^i w_i} \quad (74)$$

is used.

For formulating the weak form, the three balance equations (18), (21) and (23) (i) are multiplied by test functions δu^i , δw^i and $\delta \tilde{\alpha}$, (ii) integration over the spatial domain is performed, and (iii) the Gauss theorem is applied, resulting in

$$\int_{V(t)} \delta w^j_{,i} t^i_j dV(t) - \int_{\bar{A}(t)} \delta w^j \bar{t}_j d\bar{A}(t) = 0, \quad (75)$$

$$\int_{V(t)} -\delta w^j_{,i} m^i_j + \delta w^j \epsilon_{jk}{}^l t^k_l dV(t) = 0, \quad (76)$$

$$\int_{V_0} \delta \tilde{\alpha} \tilde{\alpha} + l_d^2 \delta \tilde{\alpha}_{,I} \tilde{\alpha}_{,J} G^{IJ} - \delta \tilde{\alpha} \alpha_d dV_0 = 0, \quad (77)$$

with \bar{t}_j denoting the surface traction vector acting on the boundary $\bar{A}(t)$.

Next, the weak form is discretized spatially by interpolating the three fields and their gradients from the node values, using the respective interpolation operators \mathbf{N}_A and their spatial derivatives $\mathbf{N}_{A,i}$ with subscripts $(\bullet)_A$ and $(\bullet)_B$ henceforth denoting node indices as

$$\begin{aligned} u^i &= \mathbf{N}_A \mathbf{q}^u_{A^i}, & u^i_{,j} &= \mathbf{N}_{A,j} \mathbf{q}^u_{A^i}, \\ w^i &= \mathbf{N}_A \mathbf{q}^w_{A^i}, & w^i_{,j} &= \mathbf{N}_{A,j} \mathbf{q}^w_{A^i}, \\ \tilde{\alpha} &= \mathbf{N}_A \mathbf{q}^\alpha_A, & \tilde{\alpha}_{,I} &= \mathbf{N}_{A,I} \mathbf{q}^\alpha_A, \end{aligned} \quad (78)$$

using transformation

$$\mathbf{N}_{A,j} = \mathbf{N}_{A,J} F^{-1J}{}_j. \quad (79)$$

with $\mathbf{q}^u_{A^i}$, $\mathbf{q}^w_{A^i}$ and \mathbf{q}^α_A denoting the vectors of the node values of the displacement field u^i , the microrotation field in terms of the components of the axial vector w^i , and the field of the damage-driving variable $\tilde{\alpha}$, respectively, and assuming identical interpolation for all fields for the sake of simplicity. Similarly, employing the Bubnov-Galerkin approach, test functions δu^i , δw^i and $\delta \tilde{\alpha}$, and their respective gradients are interpolated using the same interpolation operators \mathbf{N}_A and $\mathbf{N}_{A,J}$. Accordingly, the discretized weak form is expressed using the Kirchhoff stress, $\tau^i_j = J t^i_j$, the Kirchhoff couple stress $\mu^i_j = J m^i_j$ and local

damage driving variable α_d as

$$\delta \mathbf{q}_A^u{}^j \left(\int_{V_0} \mathbf{N}_{A,i} \tau_j^i dV_0 - \int_{\bar{A}} \mathbf{N}_A \bar{t}_j d\bar{A} \right) = \delta \mathbf{q}_A^u{}^j \mathbf{r}_{Aj}^u = 0, \quad (80)$$

$$\delta \mathbf{q}_A^w{}^j \int_{V_0} (-\mathbf{N}_{A,i} \mu_j^i + \mathbf{N}_A \epsilon_{jk}{}^l \tau_l^k) dV_0 = \delta \mathbf{q}_A^w{}^j \mathbf{r}_{Aj}^w = 0, \quad (81)$$

$$\delta \mathbf{q}_A^\alpha \int_{V_0} \mathbf{N}_A \tilde{\alpha} + (l_d)^2 \mathbf{N}_{A,I} \tilde{\alpha}_{,J} G^{IJ} - \mathbf{N}_A \alpha_d dV_0 = \delta \mathbf{q}_A^\alpha \mathbf{r}_{Aj}^\alpha = 0, \quad (82)$$

in which use of (26) was made to express the integrals over the undeformed body, and with \mathbf{r}_{Aj}^u , \mathbf{r}_{Aj}^w and \mathbf{r}_{Aj}^α denoting the nodal residual vectors, which are used to assemble the nonlinear equation system. The latter is commonly solved by means of the Newton scheme, which requires the derivatives of the residual vectors with respect to the vectors of the nodal values. Those derivatives are summarized in Appendix B. Expressing the constitutive relations in terms of the Kirchhoff stress measures is in particular beneficial for an efficient numerical implementation, since the resulting expressions at finite element level become independent of the Jacobian determinant J .

In (80), (81) and (82), the Kirchhoff stress τ_j^i , the Kirchhoff couple stress μ_j^i and local damage driving variable α_d are considered functions of F_I^i , w^i , $w_{,I}^i$, $\tilde{\alpha}$, and the set of internal state variables α^\bullet

$$\tau_j^i = \tau_j^i(F_I^i, w^i, w_{,I}^i, \tilde{\alpha}, \alpha^\bullet), \quad \mu_j^i = \mu_j^i(F_I^i, w^i, w_{,I}^i, \tilde{\alpha}, \alpha^\bullet), \quad \alpha_d = \alpha_d(F_I^i, w^i, w_{,I}^i, \tilde{\alpha}, \alpha^\bullet), \quad (83)$$

and, accordingly, they depend on the node values $\mathbf{q}_B^u{}^k$, $\mathbf{q}_B^w{}^k$ and \mathbf{q}_B^α , and the loading history of the material.

4. Numerical implementation of the constitutive relations

At quadrature point level, the constitutive relations are computed by means of a stress update algorithm, computing in a time interval $[t_{(\text{old})}, t = t_{(\text{old})} + \Delta t]$ for the given (total) deformation state F_I^i , w^i and $w_{,I}^i$ and based on the known state of the material at time $t_{(\text{old})}$ the updated Kirchhoff stress $\tau_j^i(t)$, the updated Kirchhoff couple stress $\mu_j^i(t)$, the updated damage driving variable $\alpha_d(t)$, and the updated set of internal variables $\alpha(t)$. Additionally, the algorithmic tangents of $\tau_j^i(t)$, $\mu_j^i(t)$, and $\alpha_d(t)$ with respect to the deformation tensors are computed within the stress update algorithm for solving the global equation system, and they are summarized in Appendix C. In the following, subscript $(\bullet)_{(\text{old})}$ denotes the respective value at the beginning of the time increment, whereas an omitted subscript denotes the value of a variable at the end of the time increment, i.e., at $t = t_{(\text{old})} + \Delta t$.

4.1. Update of deformation measures

By means of the current values of F_I^i , w^i and $w_{,I}^i$, the Lagrangian set of deformation measures is computed. To this end, the computation of χ_I^i is performed in an updated manner, as described in [47], exploiting a multiplicative update of the microrotation tensor defined as

$$\chi_I^i = \Delta \chi_j^i \chi_{I(\text{old})}^j \quad (84)$$

with

$$\Delta\chi_j^i = \Delta\chi_j^i(\Delta w^i) \quad (85)$$

taking the increment of the axial vector $\Delta w^i = w^i(t) - w^i(t_{\text{old}})$ and making use of the Euler-Rodrigues formula (73) and with $\chi_{I(\text{old})}^j$ denoting the known components of the microrotation tensor at the beginning of the increment. Furthermore, the material gradient of the microrotation update is computed as

$$\Delta\chi_{j,J}^i = \frac{\partial\Delta\chi_j^i}{\partial\Delta w^i} \Delta w_{,J}^i. \quad (86)$$

Observe that this allows for an additive update scheme of the wryness tensor, as described in [25]:

$$\Gamma_I^J = \Delta\Gamma_I^J + \Gamma_{I(\text{old})}^J = -\frac{1}{2} \epsilon^J{}_{K^L} \mathfrak{X}^K{}_k \Delta\chi^k{}_{l,I} \chi^l{}_{L(\text{old})} + \Gamma_{I(\text{old})}^J. \quad (87)$$

Deformation tensor \mathfrak{C}_I^J is then computed using the current value of F_I^i by means of (84) and (5).

4.2. Integration of plastic evolution equations: elastic predictor

Along the lines of plasticity theory for the classical continuum, a trial effective Mandel stress, a trial effective Biot couple stress, and a trial state of the hardening state are computed by means of the updated deformation measures as

$$\bar{T}^{\text{tr}\bar{I}}{}_J = \rho_0 \frac{\partial\Psi}{\partial\mathfrak{C}^{\text{e, tr}\bar{I}}{}_J} \Big|_{\omega=0}, \quad \bar{M}^{\text{tr}I}{}_J = \rho_0 \frac{\partial\Psi}{\partial\Gamma^{\text{e, tr}J}{}_I} \Big|_{\omega=0}, \quad \bar{\beta}_{\bullet}^{\text{tr}} = \rho_0 \frac{\partial\Psi}{\partial\alpha_{\text{tr}}^{\bullet}} \Big|_{\omega=0} \quad (88)$$

assuming

$$\mathfrak{C}^{\text{e, tr}\bar{I}}{}_J = (F^{\text{p}})^{-1\bar{I}}{}_{\bar{I}(\text{old})} \mathfrak{C}_I^J, \quad \Gamma^{\text{e, tr}J}{}_I = \Gamma_I^J - \Gamma^{\text{p}J}{}_{I(\text{old})}, \quad \alpha_{\text{tr}}^{\bullet} = \alpha_{(\text{old})}^{\bullet}. \quad (89)$$

If $f_{\text{p}}(\bar{T}^{\text{tr}\bar{I}}{}_J, \bar{M}^{\text{tr}I}{}_J, \bar{\beta}_{\bullet}^{\text{tr}}) \leq 0$, purely (damaged-)elastic material behavior occurs, and

$$\bar{T}^{\bar{I}}{}_J = \bar{T}^{\text{tr}\bar{I}}{}_J, \quad \bar{M}^I{}_J = \bar{M}^{\text{tr}I}{}_J, \quad \alpha_{\bullet}^{\bullet} = \alpha_{(\text{old})}^{\bullet}. \quad (90)$$

4.3. Integration of plastic evolution equations: return mapping algorithm

Otherwise, i.e., if $f_{\text{p}}(\bar{T}^{\bar{I}}{}_J, \bar{M}^I{}_J, \bar{\beta}_{\bullet}) > 0$, plastic material behavior occurs, and the finite strain return mapping algorithm [43] is employed for computing the updated unknowns $\mathfrak{C}^{\text{e}\bar{I}}{}_J$, $\Gamma^{\text{e}J}{}_I$ and α_{\bullet} by solving the nonlinear equation system

$$\begin{pmatrix} \mathfrak{C}^{\text{e, tr}\bar{I}}{}_J \\ \Gamma^{\text{e, tr}J}{}_I \\ \alpha_{\text{tr}}^{\bullet} \\ 0 \end{pmatrix} = \begin{pmatrix} \mathfrak{C}^{\text{e}\bar{K}}{}_K \Delta F^{\text{p}\bar{K}}{}_{\bar{I}} \\ \Gamma^{\text{e}J}{}_I + \Delta\Gamma^{\text{p}J}{}_I \\ \alpha_{\bullet} - \Delta\alpha_{\bullet} \\ f_{\text{p}}(\bar{T}^{\bar{I}}{}_J, \bar{M}^I{}_J, \bar{\beta}_{\bullet}) \end{pmatrix}, \quad (91)$$

$$\Delta F^{\text{p}\bar{J}}{}_{\bar{I}} = \exp\left(\Delta\lambda \frac{\partial g_{\text{p}}(\bar{T}^{\bar{I}}{}_J, \bar{M}^I{}_J, \bar{\beta}_{\bullet})}{\partial\mathcal{T}^{\bar{I}}{}_J}\right), \quad (92)$$

$$\Delta\Gamma^{\text{p}J}{}_I = \Delta\lambda \frac{\partial g_{\text{p}}(\bar{T}^{\bar{I}}{}_J, \bar{M}^I{}_J, \bar{\beta}_{\bullet})}{\partial M^I{}_J}, \quad (93)$$

$$\Delta\alpha_{\bullet} = -\Delta\lambda \frac{\partial h_{\text{p}}(\bar{T}^{\bar{I}}{}_J, \bar{M}^I{}_J, \bar{\beta}_{\bullet})}{\partial\beta_{\bullet}}, \quad (94)$$

in which the exponential map integration [17, 43] is used for computing $F^{\text{p}\bar{J}}{}_{\bar{I}} = \Delta F^{\text{p}\bar{J}}{}_{\bar{I}} F^{\text{p}\bar{I}}{}_{J(\text{old})}$, and the

implicit Euler backward integration is employed for updating $\Gamma^p{}_I = \Delta\Gamma^p{}_I + \Gamma^p{}_{I(\text{old})}$ and $\alpha^\bullet = \Delta\alpha^\bullet + \alpha^\bullet_{(\text{old})}$. For the numerical implementation of the exponential map integrator, the series approximation

$$\exp\left(\Delta\lambda \frac{\partial g_p(\bar{T}^I{}_J, \bar{M}^I{}_J, \bar{\beta}^\bullet)}{\partial \mathcal{T}^I{}_J}\right) = \sum_{n=1}^{\infty} \frac{1}{n!} \left(\Delta\lambda \frac{\partial g_p(\bar{T}^I{}_J, \bar{M}^I{}_J, \bar{\beta}^\bullet)}{\partial \mathcal{T}^I{}_J}\right)^n \quad (95)$$

is exploited. Due to the general nonsymmetry of all the involved tensors, no closed form expression of the tensor exponential is possible for the micropolar continuum.

4.4. Integration of damage evolution equations

By means of the updated plastic deformation measures $F^{pJ}{}_I$ and $\Gamma^{pJ}{}_I$, local damage driving quantity α_d is updated by integration of (71) as

$$\Delta\alpha_d = \Delta\alpha_d \left(\Delta F^{pI}{}_I, \Delta\Gamma^{pJ}{}_I, \bar{\tau}^i{}_j, \bar{\mu}^i{}_j \right), \quad (96)$$

yielding

$$\alpha_d = \Delta\alpha_d + \alpha_{d(\text{old})}, \quad (97)$$

and furthermore, for given $\tilde{\alpha}$, damage parameter ω can be updated independently by integration of (70):

$$\omega = \Delta\omega(\Delta\tilde{\alpha}) + \omega_{(\text{old})}. \quad (98)$$

Finally, the Kirchhoff stress and the Kirchhoff couple stress are updated as

$$\tau^i{}_j = \rho_0 \frac{\partial \Psi^e(\mathfrak{C}^e{}_I{}^J, \Gamma^e{}_I{}^J, \omega)}{\partial \mathfrak{C}^e{}_I{}^J} F^{ei}{}_{\bar{I}} \mathfrak{X}^J{}_j, \quad \mu^i{}_j = \rho_0 \frac{\partial \Psi^e(\mathfrak{C}^e{}_I{}^J, \Gamma^e{}_I{}^J, \omega)}{\partial \Gamma^e{}_I{}^J} F^i{}_I \mathfrak{X}^J{}_j. \quad (99)$$

For the subsequently presented realizations of the framework, the weak form and the material models were implemented by means of an implicit MOOSE [83] finite element code based application **Chamois** [73], employing the **Marmot** material modeling toolbox library [21]. The **Fastor** library [88] is used for tensor contraction operations at material and finite element level. **Fastor** enables the straightforward implementation of tensor operations using the Einstein summation notation.

5. A damaged hyper-elastic micropolar Drucker-Prager model for sandstone

A first realization of the proposed gradient-enhanced micropolar continuum framework is proposed in terms of a damage-plasticity model for sandstone based on the Drucker-Prager yield criterion. The model is applied and assessed in simulations of plane strain compression tests on Gosford sandstone performed by Ord et al. [77].

5.1. Model formulation

For describing hyperelastic relations within the micropolar continuum, a Neo-Hookean type model inspired by the model by Ramezani et al. [89] for compressive materials is employed, using an isochoric-volumetric split for the macroscopic part, as described in, e.g., [82]. The potential function is expressed

as

$$\begin{aligned} \rho_0 \Psi^e(\mathfrak{C}_{\bar{I}}^{eJ}, \Gamma_I^{eJ}, \omega) = & g(J^e) + (1 - \omega) \frac{1}{2} \left((G + G_c) \left((J^e)^{-\frac{2}{3}} \mathfrak{C}_{\bar{I}}^{eJ} \mathfrak{C}_{\bar{I}}^{e\bar{J}} - 3 \right) - G_c \left((J^e)^{-\frac{2}{3}} \mathfrak{C}_{\bar{I}}^{eJ} \mathfrak{C}_{\bar{J}}^{e\bar{I}} - 3 \right) \right) \\ & + (1 - \omega) \frac{1}{2} \left((\hat{\gamma} + \hat{\beta}) \Gamma_I^{eJ} \Gamma_J^{eI} + (\hat{\gamma} - \hat{\beta}) \Gamma_I^{eJ} \Gamma_J^{eI} + \hat{\alpha} \Gamma_I^{eI} \Gamma_J^{eJ} \right) \end{aligned} \quad (100)$$

with ω denoting the scalar isotropic damage parameter, J^e denoting the determinant of $\mathfrak{C}_{\bar{I}}^{eJ}$, and with

$$g(J^e) = \frac{K}{8} \left((J^e)^2 + (J^e)^{-2} - 2 \right) \quad (101)$$

denoting the energy due to elastic macroscopic volumetric deformation. Accordingly, it is assumed that damage affects the complete couple stress tensor, but only the deviatoric part of the classical Cauchy stress tensor. As a consequence of the deviatoric-volumetric split of the elastic potential, the relations between the effective and nominal stress and couple stress tensors can be conveniently expressed by means of the linear relations

$$t_j^i = \Omega_{jk}^i \bar{t}^k_l, \quad m_j^i = (1 - \omega) \bar{m}_j^i \quad (102)$$

with

$$\Omega_{jk}^i = (1 - \omega) \left(\delta_k^i \delta_j^l - \frac{1}{3} \delta_j^i \delta_k^l \right) + \frac{1}{3} \delta_j^i \delta_k^l. \quad (103)$$

Identical relations follow for the nominal and the effective Mandel stress tensors, $\mathcal{T}_{\bar{J}}^{\bar{I}}$ and $\bar{\mathcal{T}}_{\bar{J}}^{\bar{I}}$, and the nominal and the effective Biot couple stress tensors, M_J^I and \bar{M}_J^I .

The 6 elastic constants, expressed in the notation by Hassanpour and Heppler [44] for consistency with [74], are the shear modulus G , the bulk modulus K , the coupling modulus G_c , and the three micropolar elastic constants $\hat{\alpha}$, $\hat{\beta}$ and $\hat{\gamma}$. The latter are commonly expressed by means of a set of derived parameters, i.e., the polar ratio

$$\psi = \frac{2\hat{\gamma}}{2\hat{\gamma} + \hat{\alpha}}, \quad (104)$$

the characteristic length for bending

$$l_b = \sqrt{\frac{\hat{\gamma} + \hat{\beta}}{4G}} \quad (105)$$

and the characteristic length for torsion

$$l_t = \sqrt{\frac{\hat{\gamma}}{G}}. \quad (106)$$

In the present contribution, the principle of bounded stiffness derived by Neff et al. [72] for the small strain regime is obeyed, yielding

$$\psi = \frac{3}{2} \quad \text{and} \quad l_t = 2l_b. \quad (107)$$

Consequently, only the length scale parameter l_b and the coupling modulus G_c remain as independent elastic parameters, together with the classical parameters G and K .

For modeling plastic material behavior by means of a single, combined yield function, the concept of generalized stress invariants [15, 68, 101], computed from both the effective Mandel and couple stress tensors, $\bar{\mathcal{T}}_{\bar{J}}^{\bar{I}}$ and \bar{M}_J^I , is employed. Following the discussion in [74], the generalized effective stress

invariants I_1 and J_2 in the finite strain regime are computed as

$$\tilde{I}_1 = \bar{\mathcal{T}}_{\bar{I}}^{\bar{I}} \quad (108)$$

and

$$\tilde{J}_2 = a_1 \bar{\mathcal{S}}_{\bar{J}}^{\bar{I}} \bar{\mathcal{S}}_{\bar{I}}^{\bar{J}} + a_2 \bar{\mathcal{S}}_{\bar{I}}^{\bar{I}} \bar{\mathcal{S}}_{\bar{I}}^{\bar{I}} + \frac{1}{(l_{J2})^2} (a_3 \bar{M}_{\bar{I}}^{\bar{I}} \bar{M}_{\bar{I}}^{\bar{J}} + a_4 \bar{M}_{\bar{I}}^{\bar{I}} \bar{M}_{\bar{I}}^{\bar{J}}) \quad (109)$$

using the deviatoric part of the effective Mandel stress tensor

$$\bar{\mathcal{S}}_{\bar{J}}^{\bar{I}} = \bar{\mathcal{T}}_{\bar{J}}^{\bar{I}} - \frac{1}{3} G_{\bar{I}}^{\bar{I}} \tilde{I}_1. \quad (110)$$

In the present work, $a_1 = 0.5$, $a_2 = 0$, $a_3 = 0.5$ and $a_4 = 0$ is assumed, consistent with [74]. Length scale parameter l_{J2} is employed for relating the different dimensions of the classical and the couple stress tensors, and it is considered a material parameter specific to the microstructure of a material.

Note that for the present model for sandstone the deviatoric-volumetric split in (100) carries over to $\bar{\mathcal{T}}_{\bar{J}}^{\bar{I}}$, yielding \tilde{I}_1 to be identical to the first invariant of the nominal Mandel stress tensor $\tilde{I}_1 = \mathcal{T}_{\bar{I}}^{\bar{I}}$, since the hydrostatic stress is independent of ω . This, however, is not the case for different effective-nominal stress relationships, e.g., such as the one employed for the model for concrete presented in Section 6.

By means of the generalized invariants, the yield function is expressed as

$$f_p(\bar{\mathcal{T}}_{\bar{J}}^{\bar{I}}, \bar{M}_{\bar{I}}^{\bar{I}}, \bar{\beta}_p) = \sqrt{\frac{3}{2}} \tilde{\rho} + \sqrt{3} (m_\phi \tilde{\mathcal{T}}_m - \beta_0) - \bar{\beta}_p \quad (111)$$

using

$$\begin{aligned} \tilde{\mathcal{T}}_m &= \frac{1}{3} \tilde{I}_1 \\ \tilde{\rho} &= \sqrt{2 \tilde{J}_2}, \end{aligned} \quad (112)$$

and with m_ϕ denoting the friction parameter, β_0 denoting the cohesion strength parameter, and $\bar{\beta}_p = (1 - \omega) \bar{\beta}_p$ denoting the nominal scalar stress like hardening parameter, related to the conjugate equivalent plastic deformation measure α_p as

$$\bar{\beta}_p = (1 - \omega) \rho_0 \frac{\partial \Psi^h}{\partial \alpha_p}, \quad \text{with} \quad \rho_0 \Psi^h = h_\Delta \left(\alpha_p + \frac{\exp(-\alpha_p h_{\text{exp}}) - 1}{h_{\text{exp}}} \right) \quad (113)$$

and with h_Δ and h_{exp} denoting hardening material parameters.

For describing the evolution of $F^p{}_{\bar{I}}$, $\Gamma^p{}_{\bar{I}}$ and α_p , the flow rules

$$L^p{}_{\bar{I}} = \dot{\lambda} \frac{\partial g_p(\bar{\mathcal{T}}_{\bar{J}}^{\bar{I}}, \bar{M}_{\bar{I}}^{\bar{I}})}{\partial \mathcal{T}_{\bar{I}}^{\bar{I}}}, \quad \dot{\Gamma}^p{}_{\bar{I}} = \dot{\lambda} \frac{\partial g_p(\bar{\mathcal{T}}_{\bar{J}}^{\bar{I}}, \bar{M}_{\bar{I}}^{\bar{I}})}{\partial M_{\bar{I}}^{\bar{I}}}, \quad \dot{\alpha}_p = -\dot{\lambda} \frac{\partial f_p(\bar{\mathcal{T}}_{\bar{J}}^{\bar{I}}, \bar{M}_{\bar{I}}^{\bar{I}}, \bar{\beta}_p)}{\partial \beta_p}, \quad (114)$$

are employed, with the non-associated plastic potential function $g_p(\bar{\mathcal{T}}_{\bar{J}}^{\bar{I}}, \bar{M}_{\bar{I}}^{\bar{I}}, \beta_\psi)$ defined as

$$g_p(\bar{\mathcal{T}}_{\bar{J}}^{\bar{I}}, \bar{M}_{\bar{I}}^{\bar{I}}) = \sqrt{\frac{3}{2}} \tilde{\rho} + \sqrt{3} \left(m_\psi \tilde{\mathcal{T}}_m \frac{\beta_\psi}{(1 - \omega)} \right). \quad (115)$$

Therein, m_ψ denotes the dilation parameter, and β_ψ is a dimensionless parameter for describing a decrease in dilation depending on the hardening state as

$$\beta_\psi = 1 - \exp(-\alpha_p h_d) \quad (116)$$

with material parameter h_d .

Remark: Due to an identical dependency of $\tilde{\rho}$, $\tilde{\beta}_p$, and the term involving the hydrostatic stress \tilde{T}_m in (115) on the damage parameter ω , for the numerical implementation the return mapping algorithm can be formulated completely independent of the current state of ω up to a constant multiplied with the Lagrangian multiplier $\dot{\lambda}$, which is, however, not required to be determined explicitly in practice.

Cohesion, friction and dilation parameters β_0 , m_ϕ and m_ψ in (111) and (115) are computed as

$$\beta_0 = \frac{6c \cos(\phi)}{\sqrt{3}(3 + A \sin \phi)}, \quad m_\phi = \frac{6 \sin(\phi)}{\sqrt{3}(3 + A \sin \phi)}, \quad m_\psi = \frac{6 \sin(\psi)}{\sqrt{3}(3 + A \sin \psi)} \quad (117)$$

in which c denotes the cohesion stress like material parameter, ϕ the friction angle, ψ the angle of dilation and $-1 \leq A \leq 1$ is a fitting parameter for adjusting the Drucker-Prager yield surface for in- ($A = 1$) or circumscribing ($A = -1$) the Mohr-Coulomb yield surface.

For modeling the evolution of material damage, an exponential softening law

$$\omega = 1 - \exp\left(-\frac{\tilde{\alpha}}{\varepsilon_f}\right) \quad (118)$$

is employed, with ε_f denoting the softening modulus, and the local damage driving field α_d is driven by the accumulation of the inelastic volumetric deformation as

$$\dot{\alpha}_d = \frac{D}{Dt} \left(\log \left(\det F^{pI} \right) \right) \quad (119)$$

To ensure $\dot{\alpha}_d \geq 0$, the current model is restricted to non-contractant material behavior only, i.e., $\psi \geq 0$ must be satisfied. This way, a monotonic growth of damage ω ensured.

5.2. Application to plane strain tests by Ord et al.

The proposed model is calibrated and assessed by means of the experimental tests on Gosford sandstone performed by Ord et al. [77]. During this experimental study, prismatic sandstone specimens with dimensions of 80 mm × 40 mm × 80 mm were subjected to vertical compression under plane strain conditions, employing different magnitudes of lateral confining pressures ranging from 0 MPa to 20 MPa. During the tests, the primarily observed failure mode was shear failure, characterized by the emergence of a diagonal shear band across the specimens. The numerical treatment of the emergence of shear bands in those tests has been investigated previously by Regueiro and Borja [91] using a strong discontinuity approach. Herein, it is demonstrated that the proposed gradient-enhanced micropolar approach naturally captures emerging shear bands in a continuum setting, and it provides a sound framework for describing the complex kinematics in those zones of localized deformations.

For investigating the proposed model, the tests are simulated by means of an equivalent 2D plane strain finite element model, using 8 node quadrilateral elements with a reduced Gaussian quadrature rule. For

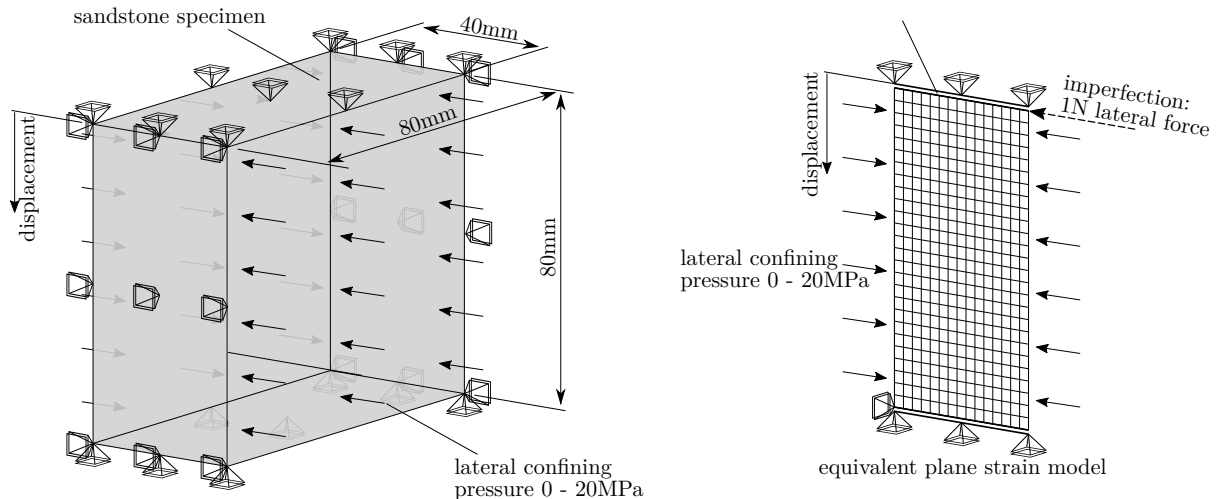


Figure 4: Experimental setup for the plane strain compression tests on Gosford sandstone by [77] (left), and equivalent plane strain finite element model using three different fine element meshes with 40×80 elements (coarse), 60×120 elements (medium), and 80×160 elements (fine), employing quadratic shape functions with a reduced quadrature rule (right).

Table 1: Material parameters for Gosford sandstone used in the plane strain compression tests by Ord et al. [77].

E (GPa)	ν (-)	G_c/G (-)	l_b (mm)	l_d (mm)	l_{J2} (mm)	c (MPa)	ϕ ($^\circ$)	ψ ($^\circ$)	A (-)	h_Δ (MPa)	h_{exp} (-)	h_d (-)	ε_f (-)
13.0	0.35	0.1	1	1	1	8.0	30	20	1	11.0	1400.0	1.0	0.11

demonstrating the mesh-insensitivity of the proposed framework, three different resolutions of the mesh are employed: 40×80 elements (coarse, 39 525 degrees of freedom), 60×120 elements (medium, 88 085 degrees of freedom), and 80×160 elements (fine, 155 845 degrees of freedom). The experimental test setup is illustrated together with the 2D finite element model in Figure 4.

Due to the homogeneous initial conditions, the location of the emerging shear band is not predefined a priori. However, in the experiments, the shear band commonly did not attain top and bottom surfaces of the specimens at which the load was applied. Hence, although polished steel plates were used for load application in order to minimize frictional effects, it is assumed that certain confining effects due friction were present. This additional confinement is simulated by constraining the top and bottom surfaces by means of a rigid body constraint, i.e., in plane relative displacements of the nodes located at those surfaces are constrained, whereas a displacement of the surface as a whole is permitted. This way, an additional confining effect is achieved in the vicinity of the top and bottom surfaces, resulting in the shear band emerging in the center of the specimen. Furthermore, a slight perturbation by means of a lateral force of 1 N acting on one corner is applied for defining a priori the direction of the shear band.

The Drucker-Prager model is calibrated by means of the results for specimen RAO636, which was subjected to a lateral confining pressure of 20 MPa, and the resulting material parameters are listed in Table 1. In particular, the length scale parameters l_b , l_{J2} and l_d are chosen to adjust the thickness of the occurring shear band to match approximately the one observed in the experiments. In [74] a strategy for determining those parameters is discussed. For the coupling modulus, for many materials experimental reports in the literature [44] estimate G_c in the order of $0.1 G$ to $1 G$. In the present work, $G_c = 0.1 G$ is assumed.

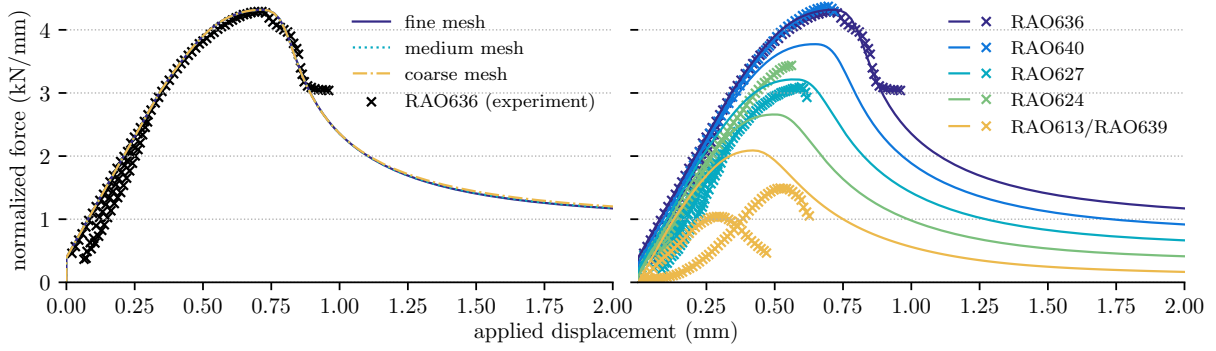


Figure 5: Experimental results and predicted load-displacement curves for the plane strain compression test on specimen RAO636 with 20 MPa lateral confining pressure using the calibrated Drucker-Prager model with the three different meshes (left), and predicted (lines) and experimental (markers) load-displacement curves for the specimens RAO636 (20 MPa), RAO640 (15 MPa), RAO627 (10 MPa), RAO624 (5 MPa), and RAO613 and RAO639 (no confining pressure) for comparison (right).

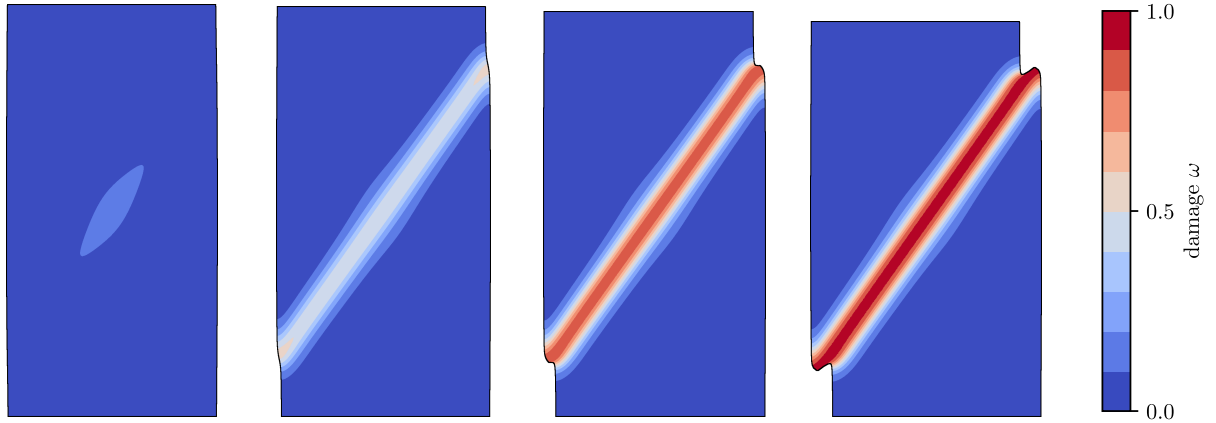


Figure 6: Evolution of material damage ω during the simulated test on specimen RAO636, at an applied vertical displacement of 0.8 mm (first), 1.0 mm (second), 2.0 mm (third), and 4.0 mm (fourth). During the test, damage and deformations localize into a narrow shear band with finite thickness.

Figure 5 (left) shows the load-displacement curve for the test on specimen RAO636 using the calibrated model, together with the respective experimental results. It can be seen that the obtained results are indeed independent of the employed finite element mesh, and they are in good agreement with the lab test results. During the test, a shear band emerges in the center of the specimen, as shown in Figure 6 by means of a contour plot of damage parameter ω . Once the shear band has emerged, additional deformations almost exclusively occur in the shear band, resulting in a zone of very large, localized inelastic deformations.

Figure 7 shows a detail of the predicted shear band for all three investigated meshes, highlighting those large deformations. It is concluded that identical to the load-displacement curve, the predicted shear band is insensitive with respect to the employed mesh, i.e., the thickness and the inclination of the shear band are identical for all meshes. For comparison, Figure 5 (right) shows the results for other specimens tested reported in [77] with lower magnitudes of the confining pressure, i.e., RAO640 (15 MPa), RAO627 (10 MPa), RAO624 (5 MPa), and RAO613 and RAO639 (no confining pressure), using the fine mesh. While it is apparent that those experimental results are characterized by considerable scatter, it

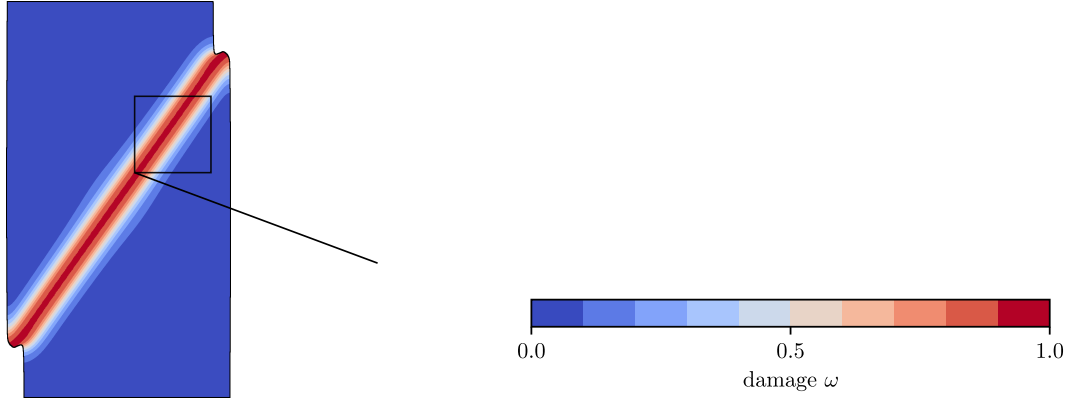


Figure 7: Detail of the predicted shear band in specimen RAO636 at an applied vertical displacement of 3 mm. For all investigated meshes (coarse, medium and fine) an identical inclination and thickness of the shear band is predicted.

is also concluded that the overall response of the material is captured reasonably well by the proposed model.

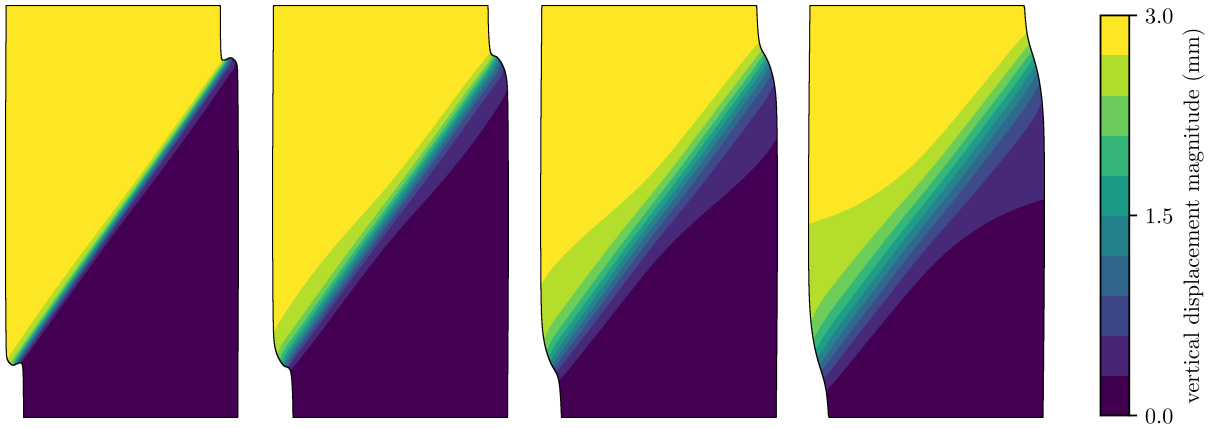


Figure 8: Illustration of the influence of the material length scale parameters l_b , l_{J_2} and l_d , on the predicted thickness of the shear band using $l_b = l_{J_2} = l_d = 1$ mm (first), $l_b = l_{J_2} = l_d = 2$ mm (second), $l_b = l_{J_2} = l_d = 3$ mm (third), $l_b = l_{J_2} = l_d = 4$ mm (fourth) for an identical applied vertical displacement of 3 mm.

The thickness of the predicted shear band is governed by the employed length scale parameters. In order to demonstrate the effect of those length scale parameters, Figure 8 shows a contour plot of the vertical displacement magnitude for different values of the length scale parameters. It can be seen that increasing values of the length parameters result in a larger thickness of the shear band. In particular for small values of the length scales, very large and localized inelastic deformations occur in the shear band, which confirms the necessity of an exact geometrical treatment.

For comparison, Figure 9 shows a photograph of the specimen RAO636 after failure in the test, with a clearly visible shear band. [Ord et al.](#) investigated the arising shear bands for different stages of the experimental tests. A micrograph of the shear band in specimen RAO640 after failure is shown in Figure 9 (right). The fracture process zone is reported with a thickness of 1 mm - 2 mm, and intergranular cracking is clearly visible. The predicted thickness of the shear band is illustrated by means of the magnitude of the microrotations. While investigating the relations between the length scale parameters and the

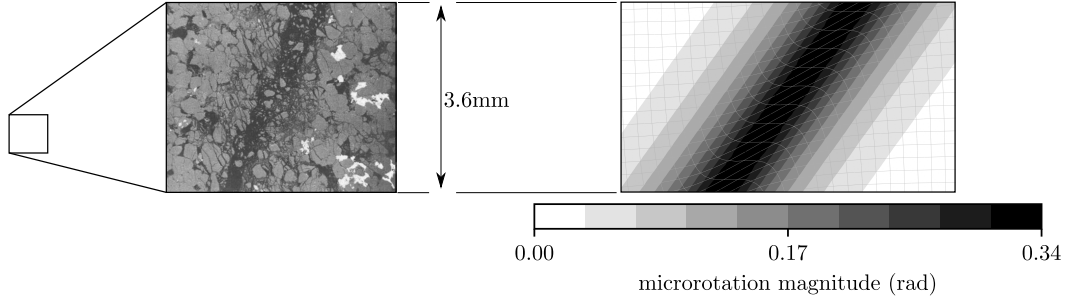


Figure 9: Observed shear band in specimen RAO636 in the tests by Ord et al. [77] with scanning electron micrograph of the shear zone in specimen RAO640 (left), and magnitude of the microrotation in the specimen at an applied vertical displacement of 2 mm using a mesh size of 160×320 elements (right), indicating the predicted thickness of the shear band for comparison. Adapted authorized reprint from [77].

microstructure is still the focus of ongoing and future research efforts, it is concluded that the predicted thickness of the shear zone is within a realistic range for the present example.

6. An extended gradient-enhanced micropolar damage-plasticity model for concrete

A second realization of the proposed geometrically exact gradient-enhanced micropolar framework is presented in terms of an extension of the Gradient-enhanced Micropolar Concrete Damage-Plasticity (GMCDP) model presented in [74] to the finite strain regime. The GMCDP model was proposed in [74] in the small strain regime as an extension of the gradient-enhanced damage-plasticity model for concrete by Grassl and Jirásek [40] and Poh and Swaddiwudhipong [87] to the micropolar continuum theory in order to provide a remedy for stability issues related to non-associated plastic flow. The performance of the GMCDP model was demonstrated by means of several benchmark examples considering different types of loading, and a comprehensive assessment of the GMCDP model compared to classical local and gradient-enhanced formulations was presented recently in [75], highlighting the advantages of the micropolar approach for modeling shear dominated failure.

For demonstrating the suitability of the proposed approach for problems different to shear failure, the extended GMCDP model is applied to an example of compressive failure with very large deformations under very high confining pressures observed in the tube-squash tests by Bažant et al. [8] as well as failure in torsion by means of the tests by Brokenshire [12].

6.1. Model formulation

For describing the elastic relations of the extended model, the hyperelastic potential

$$\rho_0 \Psi^e = \rho_0 (1 - \omega) \bar{\Psi}^e(\mathfrak{C}_I^e, \Gamma^e) \quad (120)$$

with

$$\begin{aligned} \rho_0 \bar{\Psi}^e(\mathfrak{C}_I^e, \Gamma^e) = & g(J^e) + \frac{1}{2} \left((G + Gc) \left(\mathfrak{C}_I^e \mathfrak{C}_I^e - 3 \right) - Gc \left(\mathfrak{C}_I^e \mathfrak{C}_I^e - 3 \right) \right) \\ & + \frac{1}{2} \left((\gamma + \beta) \Gamma^e \Gamma^e + (\gamma - \beta) \Gamma^e \Gamma^e + \alpha \Gamma^e \Gamma^e \right) \end{aligned} \quad (121)$$

and

$$g(J^e) = \frac{\lambda}{4} ((J^e)^2 - 1) - \left(\frac{\lambda}{2} + G \right) \ln(J^e), \quad (122)$$

by [5, 89] and with λ denoting the Lamé parameter is employed. In contrast to hyperelastic potential (120) for the sandstone model, damage parameter ω affects the complete stress tensor including the volumetric part, yielding the simple and commonly used nominal-effective relation

$$\begin{aligned} t_j^i &= (1 - \omega) \bar{t}_j^i = (1 - \omega) J^{-1} F^{ei} \mathfrak{X}_j^J \rho_0 \frac{\partial \Psi^e}{\partial \mathfrak{C}_{\bar{I}}^e}, \\ m_j^i &= (1 - \omega) \bar{m}_j^i = (1 - \omega) J^{-1} F_I^i \mathfrak{X}_j^J \rho_0 \frac{\partial \Psi^e}{\partial \Gamma_I^e}. \end{aligned} \quad (123)$$

Similar relations follow for the nominal and the effective Mandel stress tensors, $\mathcal{T}_{\bar{J}}^{\bar{I}}$ and $\bar{\mathcal{T}}_{\bar{J}}^{\bar{I}}$, and the nominal and the effective Biot couple stress tensors, M_J^I and \bar{M}_J^I .

The plasticity part of the model is formulated in terms of three invariants, i.e., the effective mean stress $\bar{\mathcal{T}}_m$ and the effective generalized deviatoric radius $\bar{\rho}$ defined in (112), and additionally the generalized Lode angle $\bar{\theta}$, defined as

$$\cos(3\bar{\theta}) = \frac{3\sqrt{3}}{2} \frac{\bar{J}_3^{\text{sym}}}{(\bar{J}_2^{\text{sym}})^{3/2}}, \quad (124)$$

with

$$\begin{aligned} \bar{J}_2^{\text{sym}} &= \frac{1}{2} \bar{\mathcal{S}}_{(\bar{J})}^{(\bar{I})} \bar{\mathcal{S}}_{(\bar{I})}^{(\bar{J})} \\ \bar{J}_3^{\text{sym}} &= \frac{1}{3} \bar{\mathcal{S}}_{(\bar{J})}^{(\bar{I})} \bar{\mathcal{S}}_{(\bar{K})}^{(\bar{J})} \bar{\mathcal{S}}_{(\bar{I})}^{(\bar{K})}, \end{aligned} \quad (125)$$

computed from the symmetric part of the deviatoric part of the Mandel stress tensor

$$\bar{\mathcal{S}}_{(\bar{J})}^{(\bar{I})} = \frac{1}{2} \left(\bar{\mathcal{S}}_{\bar{J}}^{\bar{I}} + \bar{\mathcal{S}}_{\bar{I}}^{\bar{J}} \right). \quad (126)$$

By means of those generalized invariants, a single yield function

$$f_p(\bar{\mathcal{T}}_{\bar{J}}^{\bar{I}}, \bar{M}_J^I, q_h) = \left((1 - q_h) \left(\frac{\bar{\rho}}{\sqrt{6}f_{cu}} + \frac{\bar{\mathcal{T}}_m}{f_{cu}} \right)^2 + \sqrt{\frac{3}{2}} \frac{\bar{\rho}}{f_{cu}} \right)^2 + m_0 q_h^2 \left(\frac{\bar{\rho}}{\sqrt{6}f_{cu}} r(\bar{\theta}) + \frac{\bar{\mathcal{T}}_m}{f_{cu}} \right) - q_h^2, \quad (127)$$

is used for delimiting the elastic domain. A normalized stress-like internal variable q_h is employed for describing hardening material behavior, i.e., q_h is assumed as a scalar stress like hardening parameter β in (60), keeping notation consistent with [40], defined as

$$q_h(\alpha_p) = \begin{cases} f_{cy}/f_{cu} + (1 - f_{cy}/f_{cu}) \alpha_p (\alpha_p^2 - 3\alpha_p + 3) & \text{if } \alpha_p < 1, \\ 1 & \text{otherwise,} \end{cases} \quad (128)$$

with α_p denoting the strain like hardening variable. In yield function (127), $r(\bar{\theta})$ is the Willam-Warnke [113] polar radius function, which describes the shape of the yield surface in deviatoric sections, and m_0 is the friction parameter, which depends on the material strength parameters, i.e., the uniaxial compressive strength f_{cu} , the uniaxial yield stress f_{cy} , the biaxial compressive strength f_{cb} , and the uniaxial tensile

strength f_{tu} . It is defined as

$$m_0 = 3 \frac{f_{\text{cu}}^2 - f_{\text{tu}}^2}{f_{\text{cu}} f_{\text{tu}}} \frac{e}{e+1}, \quad e = \frac{1+\epsilon}{2-\epsilon}, \quad \epsilon = \frac{f_{\text{tu}}(f_{\text{cb}}^2 - f_{\text{cu}}^2)}{f_{\text{cb}}(f_{\text{cu}}^2 - f_{\text{tu}}^2)}. \quad (129)$$

A non-associated plastic potential function

$$g_{\text{p}}(\bar{\mathcal{T}}_{\bar{J}}, \bar{M}_{\bar{J}}^I, q_{\text{h}}) = \left((1 - q_{\text{h}}) \left(\frac{\tilde{\rho}}{\sqrt{6} f_{\text{cu}}} + \frac{\tilde{\mathcal{T}}_{\text{m}}}{f_{\text{cu}}} \right)^2 + \sqrt{\frac{3}{2}} \frac{\tilde{\rho}}{f_{\text{cu}}} \right)^2 + q_{\text{h}}^2 \left(\frac{m_0 \tilde{\rho}}{\sqrt{6} f_{\text{cu}}} + \frac{m_{\text{g}}(\tilde{\mathcal{T}}_{\text{m}})}{f_{\text{cu}}} \right) \quad (130)$$

is used for describing the evolution of plastic deformation as

$$L^{\text{p}\bar{J}}_{\bar{I}} = \dot{\lambda} \frac{\partial g_{\text{p}}(\bar{\mathcal{T}}_{\bar{J}}, \bar{M}_{\bar{J}}^I, q_{\text{h}})}{\partial \bar{\mathcal{T}}_{\bar{J}}^I}, \quad \Gamma^{\text{p}J}_I = \dot{\lambda} \frac{\partial g_{\text{p}}(\bar{\mathcal{T}}_{\bar{J}}, \bar{M}_{\bar{J}}^I, q_{\text{h}})}{\partial M_{\bar{J}}^I}. \quad (131)$$

Therein, function

$$m_{\text{g}}(\tilde{\mathcal{T}}_{\text{m}}) = A_{\text{g}} B_{\text{g}} f_{\text{cu}} \exp\left(\frac{\tilde{\mathcal{T}}_{\text{m}} - f_{\text{tu}}/3}{B_{\text{g}} f_{\text{cu}}}\right), \quad (132)$$

with

$$A_{\text{g}} = \frac{3f_{\text{tu}}}{f_{\text{cu}}} + \frac{m_0}{2}, \quad (133)$$

$$B_{\text{g}} = \frac{1}{3} (1 + f_{\text{tu}}/f_{\text{cu}}) (\ln(A_{\text{g}}) - \ln(2D_{\text{f}} - 1) - \ln(3 + m_0/2) + \ln(D_{\text{f}} + 1))^{-1}, \quad (134)$$

formulated by means of dilatancy model parameter D_{f} , controls the evolution of the volumetric plastic strain.

The evolution of α_{p} is directly postulated by means of the evolution law by Unteregger et al. [107]

$$\dot{\alpha}_{\text{p}} = h_{\text{p}}(L^{\text{p}\bar{J}}_{\bar{I}}, \tilde{\mathcal{T}}_{\text{m}}, \tilde{\rho}, \tilde{\theta}) = \left\| L^{\text{p}\bar{J}}_{\bar{I}} \right\| \frac{1}{x_{\text{h}}(\tilde{\mathcal{T}}_{\text{m}})} \left(1 + 3 \frac{\tilde{\rho}^2}{\tilde{\rho}^2 + \vartheta_{\text{h}}} \cos^2(1.5\tilde{\theta}) \right), \quad (135)$$

rather than by means of a potential function, with ϑ_{h} denoting a small disturbance parameter to avoid division by zero in case of a pure hydrostatic stress. A ductility function $x_{\text{h}}(\tilde{\mathcal{T}}_{\text{m}})$ controls the magnitude of $\dot{\alpha}_{\text{p}}$ depending on the acting hydrostatic stress:

$$x_{\text{h}}(\tilde{\mathcal{T}}_{\text{m}}) = \begin{cases} A_{\text{h}} - (A_{\text{h}} - B_{\text{h}}) \exp\left(\frac{-R_{\text{h}}(\tilde{\mathcal{T}}_{\text{m}})}{C_{\text{h}}}\right) & \text{if } R_{\text{h}}(\tilde{\mathcal{T}}_{\text{m}}) \geq 0, \\ (B_{\text{h}} - D_{\text{h}}) \exp\left(\frac{R_{\text{h}}(\tilde{\mathcal{T}}_{\text{m}})(A_{\text{h}} - B_{\text{h}})}{(B_{\text{h}} - D_{\text{h}}) C_{\text{h}}}\right) + D_{\text{h}} & \text{otherwise,} \end{cases} \quad (136)$$

$$R_{\text{h}}(\tilde{\mathcal{T}}_{\text{m}}) = -\frac{\tilde{\mathcal{T}}_{\text{m}}}{f_{\text{cu}}} - \frac{1}{3},$$

formulated in terms of the model parameters A_{h} , B_{h} , C_{h} and D_{h} .

For relating the damage parameter ω to the nonlocal damage-driving variable $\tilde{\alpha}$, the exponential

softening law

$$\omega = 1 - \exp\left(-\frac{\tilde{\alpha}}{\varepsilon_f}\right) \quad (137)$$

is used, in which ε_f is the softening modulus, controlling the slope of the softening curve.

The evolution of the strain-like damage-driving variable α_d in (71), the local counterpart to $\tilde{\alpha}$ in (23), is related to the rate of the volumetric plastic deformation as

$$\dot{\alpha}_d = \begin{cases} 0 & \text{if } \alpha_p < 1, \\ \dot{\varepsilon}_V^p / x_s(\dot{\varepsilon}_{IJ}^p) & \text{otherwise.} \end{cases} \quad (138)$$

with ε_{IJ}^p denoting the logarithmic plastic strain tensor

$$\varepsilon_{IJ}^p = \frac{1}{2} \ln \left(F^{p\bar{I}} G_{\bar{I}\bar{J}} F^{p\bar{J}} \right) \quad (139)$$

and

$$\dot{\varepsilon}_V^p = \dot{\varepsilon}_{IJ}^p G^{IJ}. \quad (140)$$

Function $x_s(\dot{\varepsilon}_{IJ}^p)$ represents a ductility measure to account for brittle behavior in tension and ductile behavior in compression:

$$x_s(\dot{\varepsilon}_{IJ}^p) = \begin{cases} 1 + A_s R_s^2(\dot{\varepsilon}_{IJ}^p) & \text{if } R_s(\dot{\varepsilon}_{IJ}^p) < 1, \\ 1 - 3A_s + 4A_s \sqrt{R_s(\dot{\varepsilon}_{IJ}^p)} & \text{otherwise.} \end{cases} \quad (141)$$

Therein, A_s is a material parameter, which controls ductility in compression, and function $R_s(\dot{\varepsilon}_{IJ}^p)$ denotes the ratio of the *negative* volumetric plastic logarithmic rate $\dot{\varepsilon}_V^{p\ominus}$ to the total volumetric plastic logarithmic strain rate $\dot{\varepsilon}_V^p$ as

$$R_s(\dot{\varepsilon}_{IJ}^p) = \frac{\dot{\varepsilon}_V^{p\ominus}}{\dot{\varepsilon}_V^p}, \quad (142)$$

in which $\dot{\varepsilon}_V^{p\ominus}$ is computed from the principal values $\dot{\varepsilon}_1^p$, $\dot{\varepsilon}_2^p$ and $\dot{\varepsilon}_3^p$ of the rate of the plastic logarithmic strain tensor

$$\dot{\varepsilon}_V^{p\ominus} = \langle -\dot{\varepsilon}_1^p \rangle + \langle -\dot{\varepsilon}_2^p \rangle + \langle -\dot{\varepsilon}_3^p \rangle, \quad (143)$$

and with $\langle \bullet \rangle$ denoting the Macaulay brackets.

The finite strain GMCDP model is formulated by means the same model parameters A_h , B_h , C_h , D_h , D_f as the CDP model originally proposed by Grassl and Jirásek [40], who proposed as set of default values in absence of experimental results, and they are summarized in Table 2.

Table 2: Default model parameters according to Grassl and Jirásek [40].

A_h	B_h	C_h	D_h	D_f
0.08	0.003	2.0	1×10^{-6}	0.85

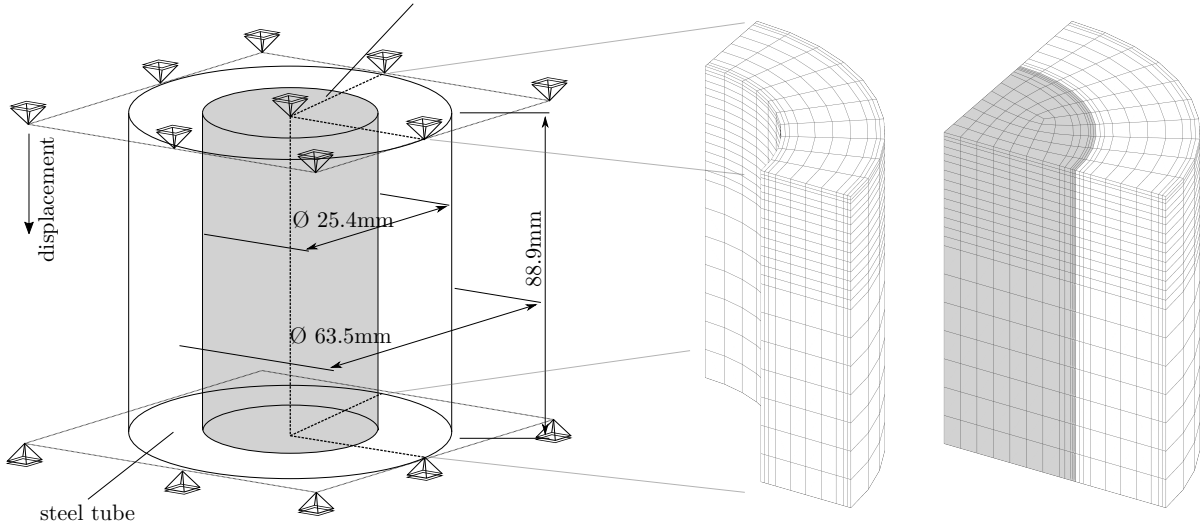


Figure 10: Setup for the tube-squash test after Bažant et al. [8] (left), and employed finite element meshes (right) for the simulations of the compression test of the empty tube and the tube filled with concrete. For the mesh, 20 node hexahedral elements with a reduced quadrature rule are used for both concrete (grey) and the steel (white).

6.2. Application to the tube-squash test on concrete cylinders by Bažant et al.

The tube-squash test by Bažant et al. [8] aims at the investigation of concrete subjected to large deformations under very high confining pressures. Under very high confining pressures, concrete can sustain considerable deformations without apparent damage or fracture. In detail, the experimental setup of the tube-squash test consists of a thick walled steel tube, which encases a concrete cylinder, as shown in Figure 10 (left). During the test, the concrete cylinder and steel tube are subjected to a displacement controlled load in axial direction, which can amount up to 50% of the initial length.

Bažant et al. [8] performed tests on different materials, including normal strength and high strength concrete. For assessing the finite strain GMCDP model, the tests on normal strength concrete cylinders with dimensions of $\varnothing 25.4 \text{ mm} \times 88.9 \text{ mm}$ are chosen. The investigated concrete composition is characterized by a uniaxial compressive strength of 41.37 MPa. Based on the guidelines [31], a specific mode fracture energy of 142.66 Nm/m^2 is determined from the uniaxial compressive strength for this concrete composition. The length scale parameters of the concrete model, l_b , l_{J2} and l_d , are chosen in accordance with previous numerical studies [45, 74, 75]. Accordingly, a softening modulus $\varepsilon_f = 0.007$ together with $l_d = 2 \text{ mm}$ for the finite strain GMCDP model is calibrated to obtain a fracture energy of 142.66 Nm/m^2 in a direct uniaxial tension test. Since no further material parameters are provided in [8], the remaining material parameters are chosen in accordance with [40] for concrete compositions of a similar grade, and they are summarized in Table 3.

Table 3: Material parameters for the concrete used in the tube-squash tests by Bažant et al. [8].

E (GPa)	ν (-)	G_c/G (-)	l_b (mm)	l_d (mm)	l_{J2} (mm)	f_{cu} (MPa)	f_{cy} (MPa)	f_{tu} (MPa)	f_{cb} (MPa)	A_s (-)	ε_f (-)
30.0	0.2	0.1	2	2	2	41.37	13.0	4.2	47	0.75	0.007

During the test, the surrounding steel tube is subjected to considerable deformations, and accordingly,

E (GPa)	ν (-)	G_c/G (-)	l_b (mm)	l_{J2} (mm)	f_y (MPa)	$h_{\text{lin}}^{(s)}$ (MPa)	$h_{\text{exp}}^{(s)}$ (-)	$f_{y,\text{exp}}$ (MPa)
210	0.3	0.1	0.1	20	250	120	8	380

inelastic material behavior occurs. For representing inelastic material behavior of steel in the numerical model, the steel tube is modeled by means of a finite strain isotropic hardening hyperelastic-plastic material model. It is formulated within the proposed gradient-enhanced micropolar framework, however, neglecting material damage. Thereby, the hyperelastic potential (121) is used, and a yield surface described by the von Mises yield criterion as

$$f_p(\mathcal{T}_J^I, M_J^I, \beta_p) = \sqrt{\frac{3}{2}} \tilde{\rho} - f_y^{(s)} - \beta_p, \quad (144)$$

with $f_y^{(s)}$ denoting the yield stress. Hardening parameter β_p is derived from a quadratic-exponential hardening potential as

$$\beta_p = \rho_0 \frac{\partial \Psi^p}{\partial \alpha_p} \quad \text{with } \rho_0 \Psi^p = \frac{1}{2} \alpha_p^2 h_{\text{lin}}^{(s)} + f_{y,\text{exp}} \left(\alpha_p + \frac{\exp(-h_{\text{exp}}^{(s)} \alpha_p) - 1}{h_{\text{exp}}^{(s)}} \right), \quad (145)$$

and an associated flow rule is employed as

$$L^p \bar{I} = \dot{\lambda} \frac{\partial f_p(\mathcal{T}_J^I, M_J^I, \beta_p)}{\partial \mathcal{T}_J^I}, \quad \dot{\Gamma}^p J_I = \dot{\lambda} \frac{\partial f_p(\mathcal{T}_J^I, M_J^I, \beta_p)}{\partial M_J^I}, \quad \dot{\alpha}_p = -\dot{\lambda} \frac{\partial f_p(\mathcal{T}_J^I, M_J^I, \beta_p)}{\partial \beta_p} \quad (146)$$

The model is calibrated based on the experiments performed on the empty steel tubes, and the identified material parameters are summarized in Table 4.

In the finite element models, three-fold symmetry is exploited, i.e., only 1/8 of the structure is considered. The finite element meshes for the empty steel tube and the steel tube filled with concrete are shown in Figure 10 (right). For simulating the steel tube filled with concrete, a rigid bond between steel and concrete is assumed, however, no coupling of the microrotations in concrete and steel is considered. The models are characterized by 70 301 and 134 113 degrees of freedom for the empty and the filled steel tube, respectively. For application of the load, a displacement of 44.45 mm is applied.

Figure 11 (left) shows the experimental load-displacement curve for the empty steel tube together with the numerical prediction by means of the finite strain von Mises plasticity model, and Figure 12 (left) shows the contour plot of the equivalent inelastic strain $\alpha_p^{(s)}$ in the deformed steel tube. It can be seen that the response obtained by means of calibrated plasticity model is in excellent agreement with the experimentally measured structural response. During the test, the tube is bulging, resulting in considerable inelastic deformations in the center of the tube. A similar bulging of the tube was observed during the experiments in [8], as illustrated in Figure 13.

Figure 11 (right) shows the experimental load-displacement curve for the steel tube filled with concrete, together with the numerical prediction by means of the calibrated steel model and the finite strain GMCDP model. Similar to the S-shape of the experimental load-displacement curve, the predicted curve shows an increase of the load at an applied displacement of approximately 30 mm. This is the consequence of the

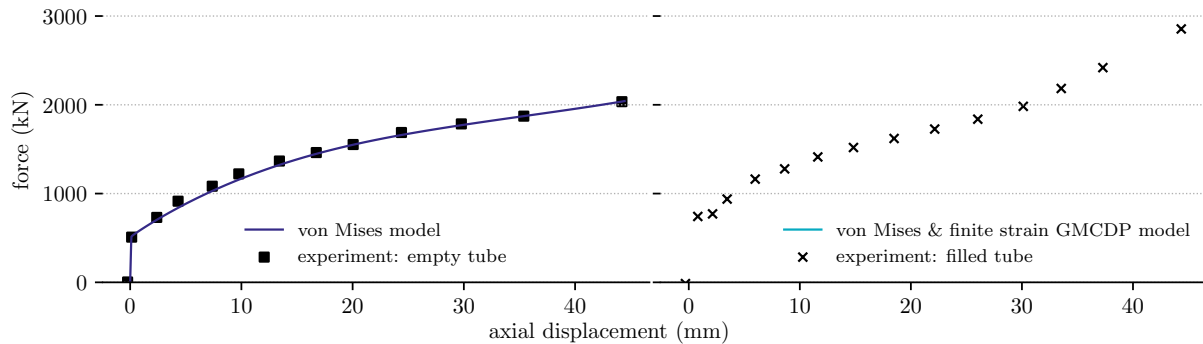


Figure 11: Load–displacement curves for the tube squash test, considering the empty tube only (left), and the tube filled with concrete (right): Experimental results by Bažant et al. [8], and respective predictions using the micropolar von Mises plasticity and the finite strain GMCDP models.

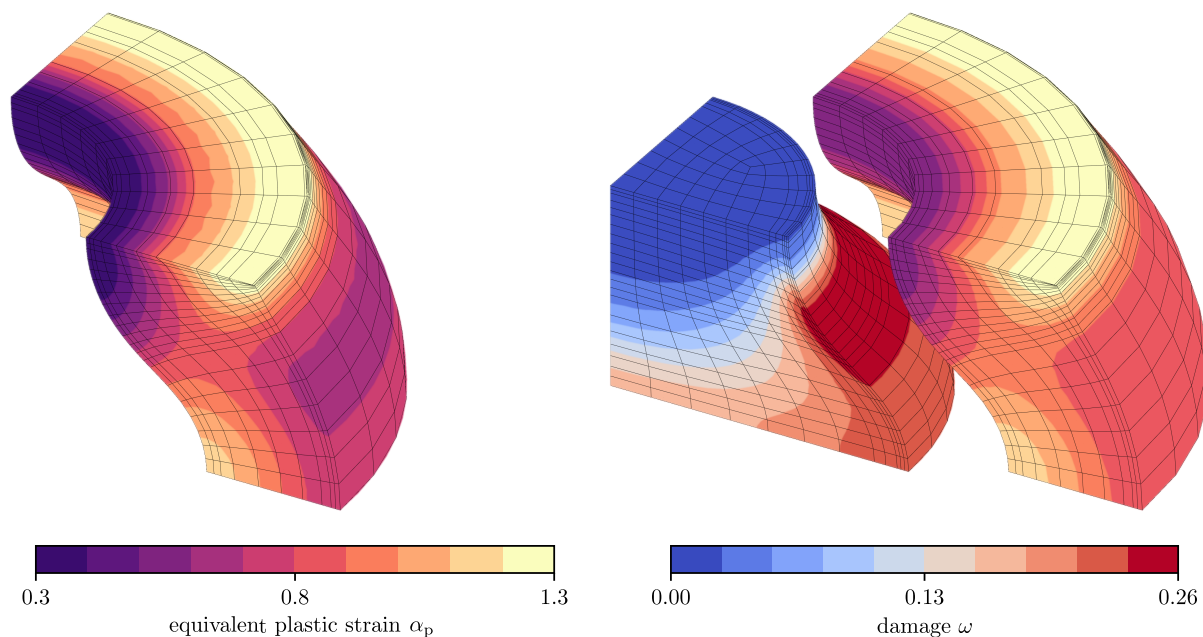


Figure 12: Predicted distribution of the equivalent plastic strain in the steel tube for the test on the empty tube only (left), and distributions of the equivalent plastic strain in the steel tube and material damage ω in the concrete for the test on the tube filled with concrete (right).

increasing lateral confining pressure during the test, enabling the concrete to sustain considerable axial loads. Considering the finite strain GMCDP model was not calibrated by means of the data of the tube-squash test, it is concluded that the blind prediction obtained by means of the GMCDP model yields excellent results.

Figure 12 (right) shows the distribution of damage ω within the concrete, together with the equivalent inelastic strain $\alpha_p^{(s)}$ in the steel tube. It can be seen that damage occurs in nearly the complete concrete specimen. However, damage attains a maximum of only 26%, indicating the very ductile behavior of concrete in the highly confined stress state predicted by the GMCDP model. For the filled steel tube, it is observed that compared to the empty tube considerably larger inelastic deformations occur in particular at



Figure 13: Steel tube before and after the tube-squash test by Bažant et al. [8] (top row), and sections (bottom row) through a deformed empty steel tube (left) and a steel tube filled with high strength concrete (right). Adapted authorized reprint from [8].

the inner surface at both ends of the tube, and at the outer surface at the center of the tube. Comparison of the deformed shape of the specimen with the one observed in the experiments (Figure 13) further confirms the predictive capabilities of the finite strain GMCDP model.

6.3. Application to the torsional tests on prismatic concrete specimens by Brokenshire

Brokenshire [12] performed a series of torsional experimental tests on prismatic and cylindrical notched concrete specimens of different grades. This test has been investigated previously e.g., using finite elements with embedded discontinuities [64] or a localizing gradient-enhanced damage model [93]. The test setup, illustrated in Figure 14, consist of a prismatic specimen with an inclined notch, which is held by two metal clamps. Each of those metal clamps has two cantilevering beams attached. During the test, three of the four ends of the cantilevering beams are in vertical direction, and a displacement controlled load is applied at the end of the fourth beam, resulting in a torsional load applied to the concrete specimen. The set performed on prismatic specimens with a uniaxial compressive strength of 40.3 MPa is employed for assessing the performance of the finite strain GMCDP model in torsion.

In the numerical model, the concrete specimen is represented by means of the finite strain GMCDP model, whereas the steel clamps are represented by means of a hyperelastic Neo-Hookean material model using the hyperelastic potential (121). Rigid bond is assumed between concrete and the steel clamps, considering no coupling of the microrotations in the steel and the concrete. For application of the load, a displacement of 10 mm is applied at the metal clamp. The finite element mesh using 20 node hexahedral elements with a reduced quadrature rule is shown in Figure 14 (right), characterized by 1 111 712 degrees of freedom in total.

For the experiments, the material properties for the concrete of grade *C40* are taken from [51]. The length scale parameters l_b , l_{j2} and l_d are chosen in accordance with previous tube squash test, and in accordance with [45, 74, 75]. Accordingly, in order to attain the specified specific mode I fracture energy of 80 Nm/m² in a uniaxial tension test, a softening modulus of $\varepsilon_f = 0.0045$ is employed. The employed

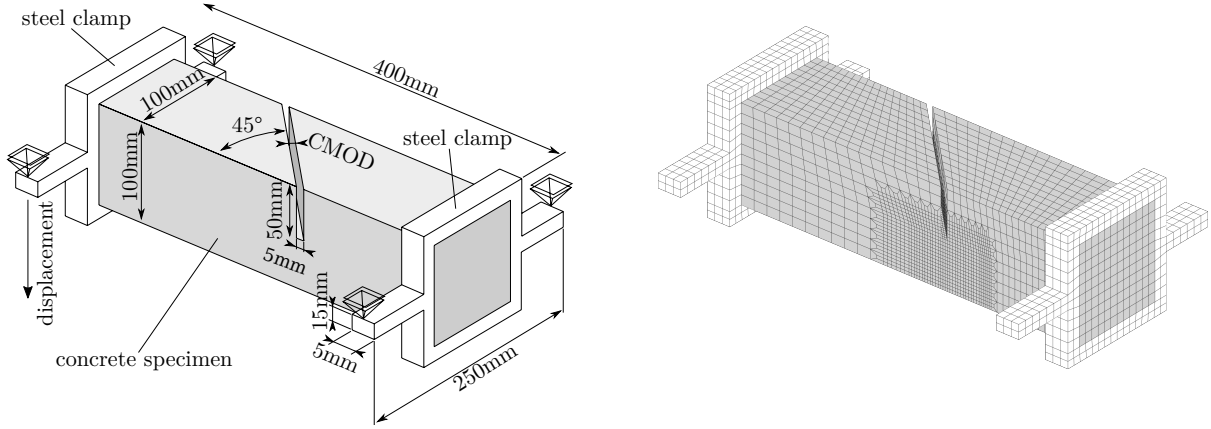


Figure 14: Setup of the torsional test on a prismatic concrete specimen after Brokenshire [12] (left) and employed finite element mesh (right). For the finite element mesh, 20 node hexahedral elements with a reduced quadrature rule are used for both concrete (grey) and the steel clamps (white).

material parameters are summarized in Table 5.

For the steel clamps, the same model as for the tube-squash test is employed, assuming a Young's modulus of $E = 210\,000$ MPa and a Poisson's ratio of $\nu = 0.3$. In contrast to the tube-squash test, no inelastic deformation occurs in the steel during the test.

Table 5: Material parameters for the experimental tests by Brokenshire [12].

E (GPa)	ν (-)	G_c/G (-)	l_b (mm)	l_d (mm)	l_{J2} (mm)	f_{cu} (MPa)	f_{cy} (MPa)	f_{tu} (MPa)	f_{cb} (MPa)	A_s (-)	ε_f (-)
34.9	0.2	0.1	2	2	2	40.3	13.0	2.83	46	0.75	0.0045

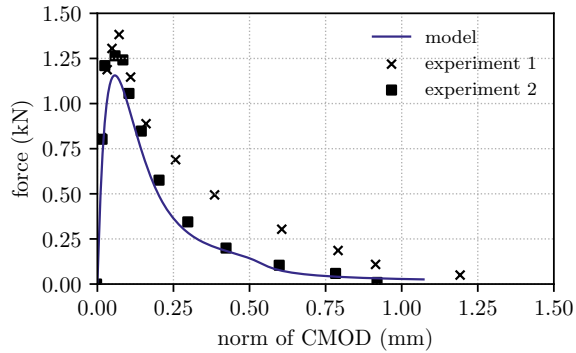


Figure 15: Predicted load–crack mouth opening displacement (CMOD) curve and experimental results from two tests by Brokenshire [12]

Figure 15 shows the predicted load–crack mouth opening displacement (CMOD) curve in comparison with the results from two experiments by Brokenshire [12]. It can be seen that the prediction is in good agreement with both experimental curves, although peak load is slightly underestimated. By contrast, the very ductile post peak response characterized by a long tail of the load–CMOD curve is captured excellently by the GMCDP model, confirming the good performance for modeling failure in torsion.

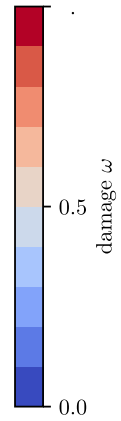


Figure 16: Damage in the prismatic concrete specimen subjected to a torsional load at an applied displacement of 10 mm.

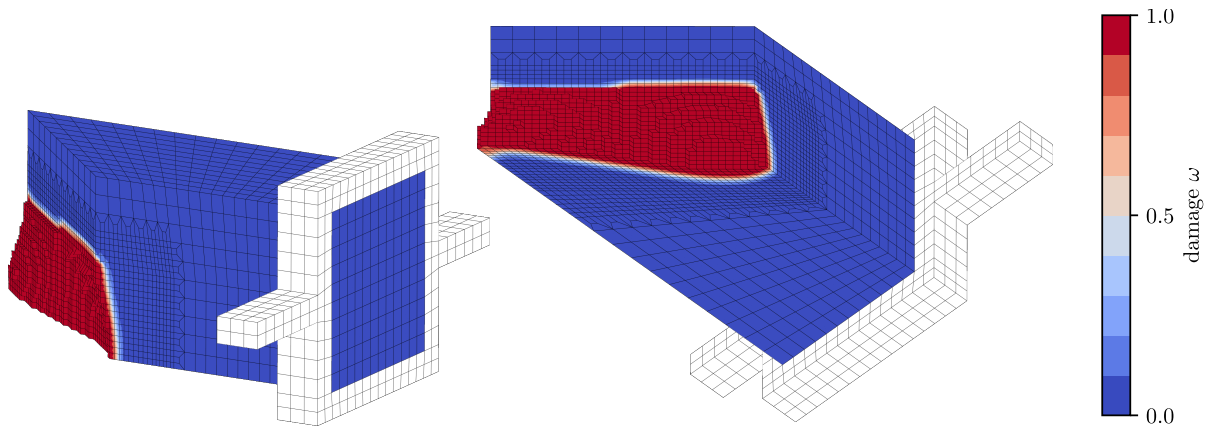


Figure 17: Detail of the predicted non-planar crack surface in the concrete specimen at an applied displacement of 10 mm.

Furthermore, Figure 16 depicts the predicted damage distribution within the specimen: Similar to the experiments, an inclined crack occurs, which separates the specimen into two parts of approximately equal size. The crack surface is highlighted in detail in Figure 17, indicating its non planar shape. This predicted shape is in excellent agreement with the experimentally observed crack reported in [51] and shown in Figure 18.

7. Conclusions and Outlook

In this work, a novel unified gradient-enhanced micropolar continuum framework for quasi-brittle cracking and shear failure of cohesive-frictional materials, formulated in the finite strain regime, has been proposed. The framework is based on a multiplicative decomposition of the macroscopic deformation gradient, and an additive decomposition of the gradient of the microrotation tensor. The balance and constitutive relations have been presented in a thermodynamically consistent manner, and details on the numerical implementation within the finite element method were discussed, both at element and quadrature point levels.

The performance and predictive capabilities of the framework were demonstrated by means of two

Figure 18: Separated parts of a prismatic concrete specimen subjected to torsion in the experiments by Brokenshire [12]. Authorized reprint from [51].

realizations of the framework in terms of a Drucker-Prager based model for sandstone, and an extended damage-plasticity model for concrete. Based on benchmark examples taken from the literature, and a comparison with experimental results, it was shown that the framework is suitable for modeling different types of material failure, i.e., shear band dominated failure, and ductile failure in confined compression and cracking in torsion. The proposed framework accounts for the characteristic length scales related to the heterogeneous microstructure of cohesive-frictional materials, which dominate the localization zone during softening. While the experimental determination of those length scale parameters is still a focus of ongoing and future research activities, it is concluded that the proposed framework is a step forward towards improved, length-scale-dependent material models.

An interesting potential application of the proposed framework for geomaterials is the incorporation of a multi-phase approach, accounting for the porous microstructure filled with liquid and/or gas. This way, the mechanical behavior in fully and partially saturated conditions, and the influence of the hydraulic conditions on material failure, could be represented in a realistic, physical manner. Possible applications include, e.g., modeling slope failure of embankment dams and strain localization in dissipative foams.

Finally, extension of the proposed framework to the full micromorphic continuum will account for additional mechanical effects at the microscopic level, which opens the door to bridge different length scales of heterogeneous materials, i.e., the micro and the macro scale. Such endeavors are currently pending.

8. Acknowledgments

Financial support for this research was provided by the Max Kade Foundation (New York) through the Max Kade Fellowship Program, the John A. Blume Earthquake Engineering Center at Stanford University, and the Department of Energy, National Nuclear Security Administration, Predictive Science Academic Alliance Program (PSAAP) under Award Number DE-NA0003962. This support is gratefully acknowledged.

Appendix A Elastic wryness with respect to macroscopic plastic intermediate configuration

An alternative elastic-plastic split, using an elastic wryness measure defined with respect to the macroscopic stress free intermediate configuration, is outlined in the following. It is inspired by the approach by Dhużewski [20], Forest and Sievert [35], exploiting the decomposition

$$\chi^i_{L,I} = (\chi^{ei}_{L,\bar{I}} + \chi^{pi}_{L,\bar{I}}) F^{p\bar{I}}_I, \quad (147)$$

with $\chi^{ei}_{L,\bar{I}}$ denoting the elastic gradient of the microdeformation field and $\chi^{pi}_{L,\bar{I}}$ the plastic gradient, defined with respect to the stress free macroscopic intermediate configuration. This yields a set of wryness tensors defined with respect to the plastic intermediate configuration

$$\hat{\Gamma}^J_{\bar{I}} = \Gamma^J_I (F^p)^{-1\bar{I}}_{\bar{I}} = \hat{\Gamma}^eJ_{\bar{I}} + \hat{\Gamma}^pJ_{\bar{I}} \quad (148)$$

with

$$\begin{aligned} \hat{\Gamma}^eJ_{\bar{I}} &= \Gamma^{eJ}_I (F^p)^{-1\bar{I}}_{\bar{I}}, \\ \hat{\Gamma}^pJ_{\bar{I}} &= \Gamma^{pJ}_I (F^p)^{-1\bar{I}}_{\bar{I}}. \end{aligned} \quad (149)$$

Then, departing from (17),

$$\begin{aligned} b^j_i &= \left(\hat{\Gamma}^eJ_I + \hat{\Gamma}^pJ_I \right) F^{-1I}{}_i \chi^j_J \\ &= \left(\hat{\Gamma}^eJ_{\bar{I}} + \hat{\Gamma}^pJ_{\bar{I}} + \hat{\Gamma}^J_{\bar{K}} \dot{F}^{p\bar{K}}_{\bar{K}} (F^p)^{-1\bar{K}}_{\bar{I}} \right) (F^e)^{-1\bar{I}}{}_i \chi^j_J \\ &= \left(\hat{\Gamma}^eJ_{\bar{I}} + \hat{\Gamma}^pJ_{\bar{I}} + \hat{\Gamma}^J_{\bar{K}} L^{p\bar{K}}_{\bar{I}} \right) (F^e)^{-1\bar{I}}{}_i \chi^j_J. \end{aligned} \quad (150)$$

The Helmholtz free energy density is now considered a function of the new elastic wryness tensor $\hat{\Gamma}^eJ_{\bar{I}}$

$$\Psi = \Psi(\mathbf{c}^eJ_{\bar{I}}, \hat{\Gamma}^eJ_{\bar{I}}, \tilde{\alpha}, \tilde{\alpha}_{,I}, \omega, \alpha^\bullet), \quad (151)$$

which allows the reformulation of the dissipation inequality as

$$\begin{aligned} &\left(T^{\bar{I}}_J - \rho_0 \frac{\partial \Psi}{\partial \mathbf{c}^eJ_{\bar{I}}} \right) \dot{\mathbf{c}}^eJ_{\bar{I}} + \left(\hat{M}^{\bar{I}}_J - \rho_0 \frac{\partial \Psi}{\partial \hat{\Gamma}^eJ_{\bar{I}}} \right) \dot{\hat{\Gamma}}^eJ_{\bar{I}} + \left(\zeta - \rho_0 \frac{\partial \Psi}{\partial \tilde{\alpha}} \right) \dot{\tilde{\alpha}} + \left(\eta^I - \rho_0 \frac{\partial \Psi}{\partial \tilde{\alpha}_{,I}} \right) \dot{\tilde{\alpha}}_{,I} \\ &+ \mathcal{T}^{\bar{I}}_J L^{p\bar{J}}_{\bar{I}} + \hat{M}^{\bar{I}}_J \left(\dot{\hat{\Gamma}}^pJ_{\bar{I}} + \hat{\Gamma}^J_{\bar{K}} L^{p\bar{K}}_{\bar{I}} \right) + Y \dot{\omega} - \beta_\bullet \dot{\alpha}^\bullet \geq 0 \end{aligned} \quad (152)$$

formulated by means of the Biot couple stress tensor $\hat{M}^{\bar{I}}_J$ defined with respect to the intermediate configuration

$$\hat{M}^{\bar{I}}_J = J m^i_j (F^e)^{-1\bar{I}}{}_i \chi^j_J. \quad (153)$$

Applying the Coleman-Noll procedure, the hyperelastic relation

$$\hat{M}^{\bar{I}}_J = \rho_0 \frac{\partial \Psi}{\partial \hat{\Gamma}^{\text{e}^J}_{\bar{I}}} \quad (154)$$

is established.

However, it is more involved to ensure $\hat{M}^{\bar{I}}_J \left(\dot{\hat{\Gamma}}^{\text{p}^J}_{\bar{I}} + \hat{\Gamma}^J_{\bar{K}} L^{\text{p}\bar{K}}_{\bar{I}} \right) \geq 0$ for arbitrary loading conditions. Inspection of this term reveals that inelastic wryness effects must occur in order to satisfy the dissipation inequality for all possible rate processes, in particular for arbitrary plastic velocity gradients $L^{\text{p}\bar{K}}_{\bar{I}}$.

In order to satisfy this requirement, a trivial choice would be

$$\dot{\hat{\Gamma}}^{\text{p}^J}_{\bar{I}} = -\hat{\Gamma}^J_{\bar{K}} L^{\text{p}\bar{K}}_{\bar{I}}. \quad (155)$$

Then, the evolution of the plastic wryness tensor $\hat{\Gamma}^{\text{p}^J}_{\bar{I}}$ is uniquely defined, and no separate flow rule by analogy to (68) is employed. However, it follows that no dissipative effects for the couple part of the model are considered.

Alternatively for considering dissipative effects, an extended split can be introduced as

$$\hat{\Gamma}^J_{\bar{I}} = \Gamma^J_{\bar{I}}(F^{\text{p}})^{-1\bar{I}}_{\bar{I}} = \hat{\Gamma}^{\text{e}^J}_{\bar{I}} + \hat{\Gamma}^{\text{p}^J}_{\bar{I}} + \hat{\Gamma}^{\text{i}^J}_{\bar{I}} \quad (156)$$

with an additional *inelastic* portion $\hat{\Gamma}^{\text{i}^J}_{\bar{I}}$. Then,

$$b_{ij} = \left(\hat{\Gamma}^{\text{e}^J}_{\bar{I}} + \dot{\hat{\Gamma}}^{\text{p}^J}_{\bar{I}} + \dot{\hat{\Gamma}}^{\text{i}^J}_{\bar{I}} + \hat{\Gamma}^J_{\bar{K}} L^{\text{p}\bar{K}}_{\bar{I}} \right) (F^{\text{e}})^{-1\bar{I}}_{i\bar{I}} \chi^j_J \quad (157)$$

assuming

$$\dot{\hat{\Gamma}}^{\text{i}^J}_{\bar{I}} + \hat{\Gamma}^J_{\bar{K}} L^{\text{p}\bar{K}}_{\bar{I}} = 0 \quad (158)$$

results in the dissipation inequality

$$\begin{aligned} & \left(T^{\bar{I}}_J - \rho_0 \frac{\partial \Psi}{\partial \mathfrak{C}^{\text{e}^J}_{\bar{I}}} \right) \dot{\mathfrak{C}}^{\text{e}^J}_{\bar{I}} + \left(\hat{M}^{\bar{I}}_J - \rho_0 \frac{\partial \Psi}{\partial \hat{\Gamma}^{\text{e}^J}_{\bar{I}}} \right) \dot{\hat{\Gamma}}^{\text{e}^J}_{\bar{I}} + \left(\zeta - \rho_0 \frac{\partial \Psi}{\partial \bar{\alpha}} \right) \dot{\bar{\alpha}} + \left(\eta^{\bar{I}} - \rho_0 \frac{\partial \Psi}{\partial \bar{\alpha}_{,I}} \right) \dot{\bar{\alpha}}_{,I} \\ & + \mathcal{T}^{\bar{I}}_J L^{\text{p}\bar{J}}_{\bar{I}} + \hat{M}^{\bar{I}}_J \dot{\hat{\Gamma}}^{\text{p}^J}_{\bar{I}} + Y \dot{\omega} - \beta_{\bullet} \dot{\alpha}_{\bullet} \geq 0. \end{aligned} \quad (159)$$

This opens the door for formulating dissipative, plastic mechanisms based on the plastic wryness rate $\dot{\hat{\Gamma}}^{\text{p}^J}_{\bar{I}}$ by analogy to (68) as

$$\dot{\hat{\Gamma}}^{\text{p}^J}_{\bar{I}} = \lambda \frac{g_{\text{p}}(T^{\bar{I}}_J, \hat{M}^{\bar{I}}_J, \beta_{\bullet})}{\hat{M}^{\bar{I}}_J}, \quad (160)$$

and with

$$\hat{\Gamma}^{\text{e}^J}_{\bar{I}} = \Gamma^J_{\bar{I}}(F^{\text{p}})^{-1\bar{I}}_{\bar{I}} - \hat{\Gamma}^{\text{p}^J}_{\bar{I}} - \hat{\Gamma}^{\text{i}^J}_{\bar{I}}. \quad (161)$$

Appendix B Tangent operators at finite element level

For solving the global nonlinear equation system by means of the Newton-Raphson method, the global stiffness matrix is assembled by means of the derivatives of the nodal residual vectors \mathbf{r}_{Aj}^u , \mathbf{r}_{Aj}^w and \mathbf{r}_A^α with respect to \mathbf{q}_B^u , \mathbf{q}_B^w and \mathbf{q}_B^α :

$$\frac{\partial \mathbf{r}_{Aj}^u}{\partial \mathbf{q}_B^u} = \int_{V_0} \mathbf{N}_{A,i} \frac{\partial \tau_j^i}{\partial F_K^k} \mathbf{N}_{B,K} - \mathbf{N}_{A,k} \mathbf{N}_{B,i} \tau_j^i dV_0 - \int_{\bar{A}} \mathbf{N}_A \bar{t}_i (\delta_j^i \delta_k^l - \delta_k^i \delta_j^l) \mathbf{N}_{B,l} d\bar{A} \quad (162)$$

$$\frac{\partial \mathbf{r}_{Aj}^u}{\partial \mathbf{q}_B^w} = \int_{V_0} \mathbf{N}_{A,i} \left(\frac{\partial \tau_j^i}{\partial w^k} \mathbf{N}_{B,K} + \frac{\partial \tau_j^i}{\partial w^k} \mathbf{N}_B \right) dV_0 \quad (163)$$

$$\frac{\partial \mathbf{r}_{Aj}^u}{\partial \mathbf{q}_B^\alpha} = \int_{V_0} \mathbf{N}_{A,i} \frac{\partial \tau_j^i}{\partial \tilde{\alpha}} \mathbf{N}_B dV_0 \quad (164)$$

$$\frac{\partial \mathbf{r}_{Aj}^w}{\partial \mathbf{q}_B^u} = \int_{V_0} -\mathbf{N}_{A,i} \frac{\partial \mu_j^i}{\partial F_K^k} \mathbf{N}_{B,K} + \mathbf{N}_A \epsilon_{jm}^n \frac{\partial \tau_n^m}{\partial F_K^k} \mathbf{N}_{B,K} + \mathbf{N}_{A,k} \mathbf{N}_{B,i} \mu_j^i dV_0 \quad (165)$$

$$\frac{\partial \mathbf{r}_{Aj}^w}{\partial \mathbf{q}_B^w} = \int_{V_0} -\mathbf{N}_{A,i} \left(\frac{\partial \mu_j^i}{\partial w^k} \mathbf{N}_{B,K} + \frac{\partial \mu_j^i}{\partial w^k} \mathbf{N}_B \right) + \mathbf{N}_A \epsilon_{jm}^n \left(\frac{\partial \tau_n^m}{\partial w^k} \mathbf{N}_{B,K} + \frac{\partial \tau_n^m}{\partial w^k} \mathbf{N}_B \right) dV_0 \quad (166)$$

$$\frac{\partial \mathbf{r}_{Aj}^w}{\partial \mathbf{q}_B^\alpha} = \int_{V_0} -\mathbf{N}_{A,i} \frac{\partial \mu_j^i}{\partial \tilde{\alpha}} \mathbf{N}_B + \mathbf{N}_A \epsilon_{jm}^n \frac{\partial \tau_n^m}{\partial \tilde{\alpha}} \mathbf{N}_B dV_0 \quad (167)$$

$$\frac{\partial \mathbf{r}_A^\alpha}{\partial \mathbf{q}_B^u} = \int_{V_0} -\mathbf{N}_A \frac{\partial \alpha_d}{\partial F_K^k} \mathbf{N}_{B,K} dV_0 \quad (168)$$

$$\frac{\partial \mathbf{r}_A^\alpha}{\partial \mathbf{q}_B^w} = \int_{V_0} -\mathbf{N}_A \left(\frac{\partial \tilde{\alpha}}{\partial w^k} \mathbf{N}_{B,K} + \frac{\partial \tilde{\alpha}}{\partial w^k} \mathbf{N}_B \right) dV_0 \quad (169)$$

$$\frac{\partial \mathbf{r}_A^\alpha}{\partial \mathbf{q}_B^\alpha} = \int_{V_0} \mathbf{N}_A \mathbf{N}_B + l_d^2 \mathbf{N}_{A,i} \mathbf{N}_{B,i} - \mathbf{N}_A \frac{\partial \alpha_d}{\partial \tilde{\alpha}} \mathbf{N}_B dV_0 \quad (170)$$

Therein, $\frac{\partial \tau_j^i}{\partial F_K^k}$, $\frac{\partial \tau_j^i}{\partial w^k}$, $\frac{\partial \tau_j^i}{\partial w^k}$, $\frac{\partial \tau_j^i}{\partial \tilde{\alpha}}$, $\frac{\partial \tau_j^i}{\partial F_K^k}$, $\frac{\partial \mu_j^i}{\partial w^k}$, $\frac{\partial \mu_j^i}{\partial w^k}$, $\frac{\partial \mu_j^i}{\partial w^k}$, $\frac{\partial \mu_j^i}{\partial \tilde{\alpha}}$, $\frac{\partial \alpha_d}{\partial F_K^k}$, $\frac{\partial \alpha_d}{\partial w^k}$, $\frac{\partial \alpha_d}{\partial w^k}$, and $\frac{\partial \alpha_d}{\partial \tilde{\alpha}}$ denote the consistent tangent operators of the constitutive model, which are consistently computed within the stress update algorithm.

Appendix C Consistent tangent operators at quadrature point level

The structure of the gradient-enhanced micropolar continuum framework allows one to exploit the fact that the elastic, plastic and damage evolution equations (88) to (98) exclusively depend on the evolution of \mathfrak{C}_I^J and Γ_I^J . Hence, it is useful to express τ_j^i , μ_j^i and α_d as functions of the deformation measures \mathfrak{C}_I^J ,

Γ_I and χ_I rather than F_K , w and $w_{,K}$ by exploiting the relations

$$\begin{aligned}
\frac{\partial \tau_j^i}{\partial F_K^k} &= \frac{\partial \tau_j^i}{\partial \mathfrak{C}_M^L} \frac{\partial \mathfrak{C}_M^L}{\partial F_K^k} \\
\frac{\partial \tau_j^i}{\partial w^k} &= \frac{\partial \tau_j^i}{\partial \mathfrak{C}_M^L} \frac{\partial \mathfrak{C}_M^L}{\partial w^k} + \frac{\partial \tau_j^i}{\partial \chi_L^l} \frac{\partial \chi_L^l}{\partial w^k} + \frac{\partial \tau_j^i}{\partial \Gamma_L^M} \frac{\partial \Gamma_L^M}{\partial w^k} \\
\frac{\partial \tau_j^i}{\partial w_{,K}^k} &= \frac{\partial \tau_j^i}{\partial \Gamma_L^M} \frac{\partial \Gamma_L^M}{\partial w_{,K}^k} \\
\frac{\partial \tau_j^i}{\partial \tilde{\alpha}} &= \frac{\partial \tau_j^i}{\partial \omega} \frac{\partial \omega}{\partial \tilde{\alpha}}
\end{aligned} \tag{171}$$

for the Kirchhoff stress,

$$\begin{aligned}
\frac{\partial \mu_j^i}{\partial F_K^k} &= \frac{\partial \mu_j^i}{\partial \mathfrak{C}_M^L} \frac{\partial \mathfrak{C}_M^L}{\partial F_K^k} \\
\frac{\partial \mu_j^i}{\partial w^k} &= \frac{\partial \mu_j^i}{\partial \mathfrak{C}_M^L} \frac{\partial \mathfrak{C}_M^L}{\partial w^k} + \frac{\partial \mu_j^i}{\partial \chi_L^l} \frac{\partial \chi_L^l}{\partial w^k} + \frac{\partial \mu_j^i}{\partial \Gamma_L^M} \frac{\partial \Gamma_L^M}{\partial w^k} \\
\frac{\partial \mu_j^i}{\partial w_{,K}^k} &= \frac{\partial \mu_j^i}{\partial \Gamma_L^M} \frac{\partial \Gamma_L^M}{\partial w_{,K}^k} \\
\frac{\partial \mu_j^i}{\partial \tilde{\alpha}} &= \frac{\partial \mu_j^i}{\partial \omega} \frac{\partial \omega}{\partial \tilde{\alpha}}
\end{aligned} \tag{172}$$

for the Kirchhoff couple stress

$$\begin{aligned}
\frac{\partial \alpha_d}{\partial F_K^k} &= \frac{\partial \alpha_d}{\partial \mathfrak{C}_M^L} \frac{\partial \mathfrak{C}_M^L}{\partial F_K^k} \\
\frac{\partial \alpha_d}{\partial w^k} &= \frac{\partial \alpha_d}{\partial \mathfrak{C}_M^L} \frac{\partial \mathfrak{C}_M^L}{\partial w^k} + \frac{\partial \alpha_d}{\partial \Gamma_L^M} \frac{\partial \Gamma_L^M}{\partial w^k} \\
\frac{\partial \alpha_d}{\partial w_{,K}^k} &= \frac{\partial \alpha_d}{\partial \Gamma_L^M} \frac{\partial \Gamma_L^M}{\partial w_{,K}^k} \\
\frac{\partial \alpha_d}{\partial \tilde{\alpha}} &= 0
\end{aligned} \tag{173}$$

and for the local damage driving quantity α_d using the first and second order derivatives of (73) for computing the derivatives

$$\begin{aligned}
\frac{\partial \chi_I^i}{\partial w^k} &= \frac{\partial \Delta \chi_j^i}{\partial \Delta w^k} \chi_{I(\text{old})}^j \\
\Delta \chi_{j,K}^i &= \frac{\partial \Delta \chi_j^i}{\partial \Delta w^k} \Delta w_{,K}^k \\
\frac{\partial \Delta \chi_{j,J}^i}{\partial w^k} &= \frac{\partial^2 \Delta \chi_j^i}{\partial \Delta w^k \partial \Delta w^l} \Delta w_{,J}^l \\
\frac{\partial \Delta \chi_{j,K}^i}{\partial w_{,K}^k} &= \frac{\partial \Delta \chi_j^i}{\partial \Delta w^k} \delta_{J,K}
\end{aligned} \tag{174}$$

of (84) and (86), which are required for $\frac{M}{\partial w^k}$, $\frac{L}{\partial w^k}$, $\frac{L}{\partial w^k}$, $\frac{L}{\partial w^k}$. Then, the derivatives of the Kirchhoff stress measures and local damage driving quantity α_d with respect to the deformation measures \mathfrak{C}_M^L , χ^L , and Γ^M_L and damage ω follow as

$$\begin{aligned}\frac{\partial \tau_j^i}{\partial \mathfrak{C}_M^L} &= \frac{\partial T_J^{\bar{I}}}{\partial \mathfrak{C}_M^L} F^{\text{ei}}_{\bar{I}} \mathfrak{x}^J_j + T_J^{\bar{I}} \frac{\partial F^{\text{ei}}_{\bar{I}}}{\partial \mathfrak{C}_M^L} \mathfrak{x}^J_j \\ \frac{\partial \tau_j^i}{\partial \chi^L} &= T_J^{\bar{I}} \frac{\partial F^{\text{ei}}_{\bar{I}}}{\partial \chi^L} \mathfrak{x}^J_j + T_J^{\bar{I}} F^{\text{ei}}_{\bar{I}} g_{lj} G^{LJ} \\ \frac{\partial \tau_j^i}{\partial \Gamma^M_L} &= \frac{\partial T_J^{\bar{I}}}{\partial \Gamma^M_L} F^{\text{ei}}_{\bar{I}} \mathfrak{x}^J_j + T_J^{\bar{I}} \frac{\partial F^{\text{ei}}_{\bar{I}}}{\partial \Gamma^M_L} \mathfrak{x}^J_j \\ \frac{\partial \tau_j^i}{\partial \omega} &= \frac{\partial T_J^{\bar{I}}}{\partial \omega} F^{\text{ei}}_{\bar{I}} \mathfrak{x}^J_j\end{aligned}\tag{175}$$

for the Kirchhoff stress,

$$\begin{aligned}\frac{\partial \mu_j^i}{\partial \mathfrak{C}_M^L} &= \frac{M^I_J}{\partial \mathfrak{C}_M^L} F^i_I \mathfrak{x}^J_j + M^I_J \frac{\partial F^i_I}{\partial \mathfrak{C}_M^L} \mathfrak{x}^J_j \\ \frac{\partial \mu_j^i}{\partial \chi^L} &= M^I_J \frac{\partial F^i_I}{\partial \chi^L} \mathfrak{x}^J_j + M^I_J F^i_I g_{lj} g^{LJ} \\ \frac{\partial \mu_j^i}{\partial \Gamma^M_L} &= \frac{M^I_J}{\partial \Gamma^M_L} F^i_I \mathfrak{x}^J_j \\ \frac{\partial \mu_j^i}{\partial \omega} &= \frac{\partial M^I_J}{\partial \omega} F^i_I \mathfrak{x}^J_j\end{aligned}\tag{176}$$

for the Kirchhoff couple stress, and

$$\begin{aligned}\frac{\alpha_d}{\partial \mathfrak{C}_M^L} &= \frac{\partial \alpha_d}{\partial \Delta F^{\text{p}\bar{I}}_I} \frac{\partial \Delta F^{\text{p}\bar{I}}_I}{\partial \mathfrak{C}_M^L} + \frac{\partial \alpha_d}{\partial \Delta \Gamma^{\text{p}J}_I} \frac{\partial \Delta \Gamma^{\text{p}J}_I}{\partial \mathfrak{C}_M^L} + \frac{\partial \alpha_d}{\partial \tau_j^i} \frac{\partial \tau_j^i}{\partial \mathfrak{C}_M^L} + \frac{\partial \alpha_d}{\partial \mu_j^i} \frac{\partial \mu_j^i}{\partial \mathfrak{C}_M^L} \\ \frac{\alpha_d}{\partial \Gamma^M_L} &= \frac{\partial \alpha_d}{\partial \Delta F^{\text{p}\bar{I}}_I} \frac{\partial \Delta F^{\text{p}\bar{I}}_I}{\partial \Gamma^M_L} + \frac{\partial \alpha_d}{\partial \Delta \Gamma^{\text{p}J}_I} \frac{\partial \Delta \Gamma^{\text{p}J}_I}{\partial \Gamma^M_L} + \frac{\partial \alpha_d}{\partial \tau_j^i} \frac{\partial \tau_j^i}{\partial \Gamma^M_L} + \frac{\partial \alpha_d}{\partial \mu_j^i} \frac{\partial \mu_j^i}{\partial \Gamma^M_L}\end{aligned}\tag{177}$$

for α_d , making use of the auxiliary identities

$$\frac{\partial F^{\text{ei}}_{\bar{I}}}{\partial \mathfrak{C}_M^L} = \frac{\mathfrak{C}_I^J}{\partial \mathfrak{C}_M^L} \chi^i_j \quad \frac{\partial F^{\text{ei}}_{\bar{I}}}{\partial \chi^L} = \mathfrak{C}_I^L \delta^i_l \quad \frac{\partial F^{\text{ei}}_{\bar{I}}}{\partial \Gamma^M_L} = \frac{\mathfrak{C}_I^J}{\partial \Gamma^M_L} \chi^i_j \quad \frac{\partial F^i_I}{\partial \chi^L} = \mathfrak{C}_I^L \delta^i_l.\tag{178}$$

The derivatives of the Biot stress measures are then expressed conveniently as

$$\begin{aligned}\frac{T_J^{\bar{I}}}{\partial \mathfrak{C}_M^L} &= \rho_0 \frac{\partial^2 \Psi^e}{\partial \mathfrak{C}_I^J \partial \mathfrak{C}_N^O} \frac{\mathfrak{C}_N^O}{\partial \mathfrak{C}_M^L} & \frac{T_J^{\bar{I}}}{\partial \Gamma^M_L} &= \rho_0 \frac{\partial^2 \Psi^e}{\partial \mathfrak{C}_I^J \partial \mathfrak{C}_N^O} \frac{\mathfrak{C}_N^O}{\partial \Gamma^M_L} & \frac{T_J^{\bar{I}}}{\partial \omega} &= \rho_0 \frac{\partial^2 \Psi^e}{\partial \mathfrak{C}_I^J \partial \omega} \\ \frac{M^I_J}{\partial \mathfrak{C}_M^L} &= \rho_0 \frac{\partial^2 \Psi^e}{\partial \Gamma^e J_I \partial \Gamma^e N_O} \frac{\Gamma^e N_O}{\partial \mathfrak{C}_M^L} & \frac{M^I_J}{\partial \Gamma^M_L} &= \rho_0 \frac{\partial^2 \Psi^e}{\partial \Gamma^e J_I \partial \Gamma^e N_O} \frac{\Gamma^e N_O}{\partial \Gamma^M_L} & \frac{M^I_J}{\partial \omega} &= \rho_0 \frac{\partial^2 \Psi^e}{\partial \Gamma^e J_I \partial \omega}\end{aligned}\tag{179}$$

Note that for the elastic stiffness tensors in (179), non-chirality was assumed, i.e., mixed derivatives $\rho_0 \frac{\partial^2 \Psi^e}{\partial \mathfrak{C}_I^J \partial \Gamma^e K_L} = 0$. Similarly, the derivatives of the plastic deformation increments $\Delta F^{\text{p}\bar{I}}_J$ and $\Delta \Gamma^{\text{p}J}_I$, are

computed as

$$\begin{aligned}
\frac{\partial \Delta F^{\text{p}\bar{I}}_{\bar{J}}}{\partial \mathfrak{C}_M^L} &= \frac{\partial}{\partial \mathfrak{C}_M^L} \left(\mathfrak{C}^{\text{e, tr } I} (\mathfrak{C}^{\text{e } I})^{-1} \right) = \left((F^{\text{p}})^{-1M} \delta^J_{\bar{J}(\text{old})} - \Delta F^{\text{p}\bar{K}}_{\bar{J}} \frac{\partial \mathfrak{C}^{\text{e } \bar{K} J}}{\partial \mathfrak{C}_M^L} \right) (\mathfrak{C}^{\text{e } \bar{I} J})^{-1} \\
\frac{\partial \Delta F^{\text{p}\bar{I}}_{\bar{J}}}{\partial \Gamma^M_L} &= \frac{\partial}{\partial \Gamma^M_L} \left(\mathfrak{C}^{\text{e, tr } I} (\mathfrak{C}^{\text{e } I})^{-1} \right) = -\Delta F^{\text{p}\bar{K}}_{\bar{J}} \frac{\partial \mathfrak{C}^{\text{e } \bar{K} J}}{\partial \Gamma^M_L} (\mathfrak{C}^{\text{e } \bar{I} J})^{-1} \\
\frac{\partial \Delta \Gamma^{\text{p}J}_I}{\partial \mathfrak{C}_M^L} &= \frac{\partial}{\partial \mathfrak{C}_M^L} \left(\Gamma^{\text{e, tr } J}_I - \Gamma^{\text{e}J}_I \right) = -\frac{\partial \Gamma^{\text{e}J}_I}{\partial \mathfrak{C}_M^L} \\
\frac{\partial \Delta \Gamma^{\text{p}J}_I}{\partial \Gamma^M_L} &= \frac{\partial}{\partial \Gamma^M_L} \left(\Gamma^{\text{e, tr } J}_I - \Gamma^{\text{e}J}_I \right) = \delta^J_M \delta^L_I - \frac{\partial \Gamma^{\text{e}J}_I}{\partial \Gamma^M_L}.
\end{aligned} \tag{180}$$

The derivatives of the elastic deformation measures $\frac{\partial \mathfrak{C}^{\text{e } \bar{K} J}}{\partial \mathfrak{C}_M^L}$, $\frac{\partial \mathfrak{C}^{\text{e } \bar{K} J}}{\partial \Gamma^M_L}$, $\frac{\partial \Gamma^{\text{e}K}_J}{\partial \mathfrak{C}_M^L}$, and $\frac{\partial \Gamma^{\text{e}K}_J}{\partial \Gamma^M_L}$ are obtained as a byproduct of the return mapping algorithm from the condition

$$\frac{\partial}{\partial (\blacksquare)} \left(\left\{ \begin{array}{c} \mathfrak{C}^{\text{e, tr } J}_I \\ \Gamma^{\text{e, tr } J}_I \\ \alpha_{\text{p, tr}}^\bullet \\ 0 \end{array} \right\} - \left\{ \begin{array}{c} \mathfrak{C}^{\text{e } \bar{K} J} \Delta F^{\text{p}\bar{K}}_{\bar{I}} \\ \Gamma^{\text{e}J}_I + \Delta \Gamma^{\text{p}J}_I \\ \alpha^\bullet - \Delta \alpha^\bullet \\ f_{\text{p}}(\bar{T}^{\bar{I}}_J, \bar{M}^I_J, \bar{\beta}_\bullet) \end{array} \right\} \right) = 0 \tag{181}$$

with $(\blacksquare) = \mathfrak{C}_M^L$ and $(\blacksquare) = \Gamma^M_L$, respectively.

References

- [1] Addressi, D. (2014). A 2D Cosserat finite element based on a damage-plastic model for brittle materials. *Computers & Structures*, 135:20–31.
- [2] Adhikary, D., Mühlhaus, H.-B., and Dyskin, A. (1999). Modelling the large deformations in stratified media – the Cosserat continuum approach. *Mechanics of Cohesive-frictional Materials*, 4(3):195–213.
- [3] Anderson, W. and Lakes, R. (1994). Size effects due to Cosserat elasticity and surface damage in closed-cell poly-methacrylimide foam. *Journal of Materials Science*, 29(24):6413–6419.
- [4] Areias, P., de Sá, J. C., and António, C. C. (2003). A gradient model for finite strain elastoplasticity coupled with damage. *Finite Elements in Analysis and Design*, 39(13):1191–1235.
- [5] Bauer, S., Dettmer, W. G., Perić, D., and Schäfer, M. (2012). Micropolar hyper-elastoplasticity: Constitutive model, consistent linearization, and simulation of 3D scale effects. *International Journal for Numerical Methods in Engineering*, 91(1):39–66.
- [6] Bažant, Z. P. (1976). Instability, ductility, and size effect in strain-softening concrete. *ASCE Journal of the Engineering Mechanics Division*, 102(2):331–344.
- [7] Bažant, Z. P. (1991). Why continuum damage is nonlocal: Micromechanics arguments. *Journal of Engineering Mechanics*, 117(5):1070–1087.
- [8] Bažant, Z. P., Kim, J. J. H., and Brocca, M. (1999). Finite Strain Tube-Squash Test of Concrete at High Pressures and Shear Angles up to 70 Degrees. *Materials Journal*, 96(5):580–592.
- [9] Bažant, Z. P. and Oh, B. (1983). Crack band theory for fracture of concrete. *Materials and Structures*, 16(3):155–177.
- [10] Bažant, Z. P., Xi, Y., and Reid, S. G. (1991). Statistical size effect in quasi-brittle structures: I. Is Weibull theory applicable? *Journal of Engineering Mechanics*, 117(11):2609–2622.

- [11] Brepols, T., Wulfinghoff, S., and Reese, S. (2020). A gradient-extended two-surface damage-plasticity model for large deformations. *International Journal of Plasticity*, 129:102635.
- [12] Brokenshire, D. R. (1996). *A Study on Torsion Fracture Tests*. PhD thesis, Cardiff University.
- [13] Coleman, B. D. and Noll, W. (1963). The thermodynamics of elastic materials with heat conduction and viscosity. *Archive for Rational Mechanics and Analysis*, 13:167–178.
- [14] Cosserat, E. and Cosserat, F. (1909). *Théorie Des Corps Déformables*. A. Hermann et fils.
- [15] de Borst, R. (1991). Simulation of strain localization: A reappraisal of the Cosserat continuum. *Engineering Computations*, 8(4):317–332.
- [16] de Borst, R. and Verhoosel, C. V. (2016). Gradient damage vs phase-field approaches for fracture: Similarities and differences. *Computer Methods in Applied Mechanics and Engineering*, 312:78–94.
- [17] de Souza Neto, E. A., Peric, D., and Owen, D. R. J. (2008). *Computational Methods for Plasticity*. John Wiley & Sons, Ltd, Chichester, UK.
- [18] Di Luzio, G. and Bažant, Z. P. (2005). Spectral analysis of localization in nonlocal and over-nonlocal materials with softening plasticity or damage. *International Journal of Solids and Structures*, 42(23):6071–6100.
- [19] Dietsche, A., Steinmann, P., and Willam, K. (1993). Micropolar elastoplasticity and its role in localization. *International Journal of Plasticity*, 9(7):813–831.
- [20] Dłużewski, P. H. (1991). Finite deformations of polar media in angular coordinates. *Finite deformations of polar media in angular coordinates*, 43(6):783–793.
- [21] Dummer, A., Mader, T., Neuner, M., and Schreter, M. (2021). Marmot library. <https://github.com/MAterialMOdelingToolbox/marmot>.
- [22] Ebrahimiyan, B. and Bauer, E. (2012). Numerical simulation of the effect of interface friction of a bounding structure on shear deformation in a granular soil. *International Journal for Numerical and Analytical Methods in Geomechanics*, 36(12):1486–1506.
- [23] Ehlers, W. and Volk, W. (1997). On shear band localization phenomena of liquid-saturated granular elastoplastic porous solid materials accounting for fluid viscosity and micropolar solid rotations. *Mechanics of Cohesive-frictional Materials*, 2(4):301–320.
- [24] Ehlers, W. and Volk, W. (1998). On theoretical and numerical methods in the theory of porous media based on polar and non-polar elasto-plastic solid materials. *International Journal of Solids and Structures*, 35(34):4597–4617.
- [25] Erdelj, S. G., Jelenić, G., and Ibrahimbegović, A. (2020). Geometrically non-linear 3D finite-element analysis of micropolar continuum. *International Journal of Solids and Structures*, 202:745–764.
- [26] Eringen, A. C. (1970). Balance Laws of Micromorphic Mechanics. *International Journal of Engineering Science*, 8(10):819–828.
- [27] Eringen, A. C. (1992). Balance laws of micromorphic continua revisited. *International Journal of Engineering Science*, 30(6):805–810.
- [28] Eringen, A. C. (1999). *Microcontinuum Field Theories*. Springer New York, New York, NY.
- [29] Eringen, A. C. (2002). *Nonlocal Continuum Field Theories*. Springer, New York.
- [30] Eringen, A. C. and Suhubi, E. S. (1964). Nonlinear theory of simple micro-elastic solids—I. *International Journal of Engineering Science*, 2(2):189–203.
- [31] fib (2013). *Model Code for Concrete Structures 2010*. Wilhelm Ernst & Sohn, Verlag für Architektur und technische Wissenschaften GmbH & Co. KG.
- [32] Forest, S. (2009). Micromorphic Approach for Gradient Elasticity, Viscoplasticity, and Damage. *Journal of Engineering Mechanics*, 135(3):117–131.
- [33] Forest, S. (2016). Nonlinear regularization operators as derived from the micromorphic approach to gradient elasticity, viscoplasticity and damage. *Proceedings of the Royal Society A: Mathematical, Physical and Engineering Sciences*, 472(2188):20150755.
- [34] Forest, S., Cailletaud, G., and Sievert, R. (1997). A Cosserat theory for elastoviscoplastic single crystals at finite deformation. *Archives of Mechanics*, 49:705–736.
- [35] Forest, S. and Sievert, R. (2003). Elastoviscoplastic constitutive frameworks for generalized continua. *Acta Mechanica*, 160(1-2):71–111.

- [36] Germain, P. (1973). The Method of Virtual Power in Continuum Mechanics. Part 2: Microstructure. *SIAM Journal on Applied Mathematics*, 25(3):556–575.
- [37] Goddard, J. (2011). A note on Eringen’s moment balances. *International Journal of Engineering Science*, 49(12):1486–1493.
- [38] Grammenoudis, P. and Tsakmakis, C. (2001). Hardening rules for finite deformation micropolar plasticity: Restrictions imposed by the second law of thermodynamics and the postulate of Π ’iushin. *Continuum Mechanics and Thermodynamics*, 13(5):325–363.
- [39] Grammenoudis, P. and Tsakmakis, C. (2008). Incompatible deformations—plastic intermediate configuration. *ZAMM—Journal of Applied Mathematics and Mechanics*, 88(5):403–432.
- [40] Grassl, P. and Jirásek, M. (2006). Damage-plastic model for concrete failure. *International Journal of Solids and Structures*, 43(22-23):7166–7196.
- [41] Günther, W. (1958). Zur Statik und Kinematik des Cosseratschen Kontinuums. *Abh. Braunschweig. Wiss. Ges.*, 10(213):20.
- [42] Hasanyan, A. D. and Waas, A. M. (2018). Localization in anisotropic elastoplastic micropolar media: Application to fiber reinforced composites. *Journal of the Mechanics and Physics of Solids*, 121:1–22.
- [43] Hashiguchi, K. and Yamakawa, Y. (2012). *Introduction to Finite Strain Theory for Continuum Elasto-Plasticity*. John Wiley & Sons, Ltd, Chichester, UK.
- [44] Hassanpour, S. and Hepler, G. R. (2017). Micropolar elasticity theory: A survey of linear isotropic equations, representative notations, and experimental investigations. *Mathematics and Mechanics of Solids*, 22(2):224–242.
- [45] Hofer, P., Neuner, M., and Hofstetter, G. (2022). Comparison of classical and higher order continuum models for shear failure of concrete. In *Computational Modelling of Concrete and Concrete Structures*. CRC Press.
- [46] Hosseini, H. S., Horák, M., Zysset, P. K., and Jirásek, M. (2015). An over-nonlocal implicit gradient-enhanced damage-plastic model for trabecular bone under large compressive strains. *International Journal for Numerical Methods in Biomedical Engineering*, 31(11):n/a–n/a.
- [47] Ibrahimbegovic, A. (1997). On the choice of finite rotation parameters. *Computer Methods in Applied Mechanics and Engineering*, 149(1-4):49–71.
- [48] Indriyanto, B. R., Zreid, I., and Kaliske, M. (2019). Finite strain extension of a gradient enhanced microplane damage model for concrete at static and dynamic loading. *Engineering Fracture Mechanics*, 216:106501.
- [49] Iordache, M.-M. and Willam, K. (1998). Localized failure analysis in elastoplastic Cosserat continua. *Computer Methods in Applied Mechanics and Engineering*, 151(3-4):559–586.
- [50] Isbuga, V. and Regueiro, R. A. (2017). Finite element analysis of finite strain micromorphic Drucker-Prager plasticity. *Computers & Structures*, 193:31–43.
- [51] Jefferson, A. D., Barr, B. I. G., Bennett, T., and Hee, S. C. (2004). Three dimensional finite element simulations of fracture tests using the Craft concrete model. *Computers and Concrete*, 1(3):261–284.
- [52] Jeong, J. and Neff, P. (2010). Existence, uniqueness and stability in linear Cosserat elasticity for weakest curvature conditions. *Mathematics and Mechanics of Solids*, 15(1):78–95.
- [53] Jirásek, M. and Bažant, Z. P. (2002). *Inelastic Analysis of Structures*. John Wiley & Sons, Ltd.
- [54] Jirásek, M. and Rolshoven, S. (2009). Localization properties of strain-softening gradient plasticity models. Part I: Strain-gradient theories. *International Journal of Solids and Structures*, 46(11):2225–2238.
- [55] Johannsen, D. and Tsakmakis, C. (2019a). Micropolar plasticity. Part II: A v.Mises version of micropolar plasticity in terms of curvature tensors related by mixed transformations. *Acta Mechanica*, 230(5):1811–1823.
- [56] Johannsen, D. and Tsakmakis, C. (2019b). Micropolar plasticity—Part I: Modeling based on curvature tensors related by mixed transformations. *Acta Mechanica*, 230(5):1565–1606.
- [57] Kafadar, C. and Eringen, A. (1971). Micropolar media—I the classical theory. *International Journal of Engineering Science*, 9(3):271–305.
- [58] Koiter, W. (1964). General theorems for elastic-plastic solids. *Progress in Solid Mechanics*, 1:165–221.
- [59] Lakes, R. (1995). Experimental methods for study of Cosserat elastic solids and other generalized elastic continua. *Continuum models for materials with microstructure*, 70:1–25.
- [60] Li, X. and Tang, H. (2005). A consistent return mapping algorithm for pressure-dependent elastoplastic Cosserat

- continua and modelling of strain localisation. *Computers & Structures*, 83(1):1–10.
- [61] Liebe, T., Menzel, A., and Steinmann, P. (2003). Theory and numerics of geometrically non-linear gradient plasticity. *International Journal of Engineering Science*, 41(13-14):1603–1629.
- [62] Liebe, T. and Steinmann, P. (2002). Two strategies towards geometrically non-linear isotropic gradient damage. *Journal of the Mechanical Behavior of Materials*, 13(3-4):175–194.
- [63] Lin, J., Wu, W., and Borja, R. I. (2015). Micropolar hypoplasticity for persistent shear band in heterogeneous granular materials. *Computer Methods in Applied Mechanics and Engineering*, 289:24–43.
- [64] Linder, C. and Zhang, X. (2013). A marching cubes based failure surface propagation concept for three-dimensional finite elements with non-planar embedded strong discontinuities of higher-order kinematics. *International Journal for Numerical Methods in Engineering*, 96(6):339–372.
- [65] Lippmann, H. (1969). Eine Cosserat-Theorie des plastischen Fließens. *Acta Mechanica*, 8(3-4):255–284.
- [66] Manzari, M. T. (2004). Application of micropolar plasticity to post failure analysis in geomechanics. *International Journal for Numerical and Analytical Methods in Geomechanics*, 28(10):1011–1032.
- [67] Mindlin, R. (1963). Influence of couple-stresses on stress concentrations. *Experimental mechanics*, 3(1):1–7.
- [68] Mühlhaus, H. B. and Vardoulakis, I. (1987). The thickness of shear bands in granular materials. *Géotechnique*, 37(3):271–283.
- [69] Needleman, A. (1988). Material rate dependence and mesh sensitivity in localization problems. *Computer Methods in Applied Mechanics and Engineering*, 67(1):69–85.
- [70] Neff, P. (2006). A finite-strain elastic–plastic Cosserat theory for polycrystals with grain rotations. *International Journal of Engineering Science*, 44(8-9):574–594.
- [71] Neff, P. and Jeong, J. (2009). A new paradigm: The linear isotropic Cosserat model with conformally invariant curvature energy. *ZAMM-Journal of Applied Mathematics and Mechanics*, 89(2):107–122.
- [72] Neff, P., Jeong, J., Münch, I., and Ramézani, H. (2010). Linear Cosserat elasticity, conformal curvature and bounded stiffness. In *Mechanics of Generalized Continua*, pages 55–63. Springer.
- [73] Neuner, M. (2021). Chamois. <https://github.com/matthiasneuner/chamois>.
- [74] Neuner, M., Gammitzer, P., and Hofstetter, G. (2020). A 3D gradient-enhanced micropolar damage-plasticity approach for modeling quasi-brittle failure of cohesive-frictional materials. *Computers & Structures*, 239:106332.
- [75] Neuner, M., Hofer, P., and Hofstetter, G. (2022). On the prediction of complex shear dominated concrete failure by means of classical and higher order damage-plasticity continuum models. *Engineering Structures*, 251:113506.
- [76] Oevel, W. and Schröter, J. (1981). Balance equations for micromorphic materials. *Journal of Statistical Physics*, 25(4):645–662.
- [77] Ord, A., Vardoulakis, I., and Kajewski, R. (1991). Shear band formation in Gosford Sandstone. *International Journal of Rock Mechanics and Mining Sciences & Geomechanics Abstracts*, 28(5):397–409.
- [78] Papamichos, E. (2010). Borehole failure analysis in a sandstone under anisotropic stresses. *International Journal for Numerical and Analytical Methods in Geomechanics*, 34(6):581–603.
- [79] Pearce, C. J., Nielsen, C. V., and Bićanić, N. (2004). Gradient enhanced thermo-mechanical damage model for concrete at high temperatures including transient thermal creep. *International Journal for Numerical and Analytical Methods in Geomechanics*, 28(7-8):715–735.
- [80] Peerlings, R. H. J., Borst, R. D., Brekelmans, W. a. M., and Vree, J. H. P. D. (1996). Gradient Enhanced Damage for Quasi-Brittle Materials. *International Journal for Numerical Methods in Engineering*, 39(19):3391–3403.
- [81] Peerlings, R. H. J., Massart, T. J., and Geers, M. G. D. (2004). A thermodynamically motivated implicit gradient damage framework and its application to brick masonry cracking. *Computer methods in applied mechanics and engineering*, 193(30-32):3403–3417.
- [82] Pence, T. J. and Gou, K. (2015). On compressible versions of the incompressible neo-Hookean material. *Mathematics and Mechanics of Solids*, 20(2):157–182.
- [83] Permann, C. J., Gaston, D. R., Andrš, D., Carlsen, R. W., Kong, F., Lindsay, A. D., Miller, J. M., Peterson, J. W., Slaughter, A. E., Stogner, R. H., and Martineau, R. C. (2020). MOOSE: Enabling massively parallel multiphysics simulation. *SoftwareX*, 11:100430.
- [84] Pietruszczak, S. and Mróz, Z. (1981). Finite element analysis of deformation of strain-softening materials. *International*

- Journal for Numerical Methods in Engineering*, 17(3):327–334.
- [85] Pijaudier-Cabot, G. and Bazant, Z. P. (1987). Nonlocal damage theory. *Journal of Engineering Mechanics*, 113(10):1512–1533.
- [86] Poh, L. H. and Sun, G. (2017). Localizing gradient damage model with decreasing interactions. *International Journal for Numerical Methods in Engineering*, 110(6):503–522.
- [87] Poh, L. H. and Swaddiwudhipong, S. (2009). Over-nonlocal gradient enhanced plastic-damage model for concrete. *International Journal of Solids and Structures*, 46(25–26):4369–4378.
- [88] Poya, R., Gil, A. J., and Ortigosa, R. (2017). A high performance data parallel tensor contraction framework: Application to coupled electro-mechanics. *Computer Physics Communications*.
- [89] Ramezani, S., Naghdabadi, R., and Sohrabpour, S. (2009). Constitutive equations for micropolar hyper-elastic materials. *International Journal of Solids and Structures*, 46(14):2765–2773.
- [90] Regueiro, R. A. (2010). On finite strain micromorphic elastoplasticity. *International Journal of Solids and Structures*, 47(6):786–800.
- [91] Regueiro, R. A. and Borja, R. I. (2001). Plane strain finite element analysis of pressure sensitive plasticity with strong discontinuity. *International Journal of Solids and Structures*, 38(21):3647–3672.
- [92] Sansour, C. (1998). A theory of the elastic-viscoplastic Cosserat continuum. *Archives of Mechanics*, 50(3):577–597.
- [93] Sarkar, S., Singh, I. V., and Mishra, B. K. (2022). A simple and efficient implementation of localizing gradient damage method in COMSOL for fracture simulation. *Engineering Fracture Mechanics*, 269:108552.
- [94] Schaefer, H. (1967). Das Cosserat Kontinuum. *ZAMM-Journal of Applied Mathematics and Mechanics*, 47(8):485–498.
- [95] Schreter, M., Neuner, M., and Hofstetter, G. (2018). Evaluation of the implicit gradient-enhanced regularization of a damage-plasticity rock model. *Applied Sciences*, 8(6):1004.
- [96] Sievert, R., Forest, S., and Trostel, R. (1998). Finite deformation Cosserat-type modelling of dissipative solids and its application to crystal plasticity. *Le Journal de Physique IV*, 08(PR8):Pr8–357–Pr8–364.
- [97] Simo, J. C. and Hughes, T. J. R. (1998). *Computational Inelasticity*. Number v. 7 in Interdisciplinary Applied Mathematics. Springer, New York.
- [98] Steinmann, P. (1994). A micropolar theory of finite deformation and finite rotation multiplicative elastoplasticity. *International Journal of Solids and Structures*, 31(8):1063–1084.
- [99] Steinmann, P. (1999). Formulation and computation of geometrically non-linear gradient damage. *International Journal for Numerical Methods in Engineering*, 46(5):757–779.
- [100] Steinmann, P. and Willam, K. (1991). Localization within the Framework of Micropolar Elasto-Plasticity. In Brügger, O. S., Mannl, V., and Najar, J., editors, *Advances in Continuum Mechanics*, pages 296–313. Springer Berlin Heidelberg, Berlin, Heidelberg.
- [101] Sulem, J. and Vardoulakis, I. (1990). Bifurcation analysis of the triaxial test on rock specimens. A theoretical model for shape and size effect. *Acta Mechanica*, 83(3-4):195–212.
- [102] Sulem, J. and Vardoulakis, I. (1995). *Bifurcation Analysis in Geomechanics*. CRC Press.
- [103] Tejchman, J. and Bauer, E. (2005). FE-simulations of a direct and a true simple shear test within a polar hypoplasticity. *Computers and Geotechnics*, 32(1):1–16.
- [104] Tejchman, J. and Gudehus, G. (2001). Shearing of a narrow granular layer with polar quantities. *International Journal for Numerical and Analytical Methods in Geomechanics*, 25(1):1–28.
- [105] Tejchman, J. and Wu, W. (1993). Numerical study on patterning of shear bands in a Cosserat continuum. *Acta Mechanica*, 99(1-4):61–74.
- [106] Toupin, R. (1962). Elastic Materials with Couple-Stresses. *Archive for Rational Mechanics and Analysis*, 11(1):385–414.
- [107] Unteregger, D., Fuchs, B., and Hofstetter, G. (2015). A damage plasticity model for different types of intact rock. *International Journal of Rock Mechanics and Mining Sciences*, 80:402–411.
- [108] Vardoulakis, I. (2018). *Cosserat Continuum Mechanics: With Applications to Granular Media*, volume 87. Springer.
- [109] Voyiadjis, G. Z. and Song, Y. (2019). Strain gradient continuum plasticity theories: Theoretical, numerical and experimental investigations. *International Journal of Plasticity*, 121:21–75.
- [110] Waffenschmidt, T., Polindara, C., Menzel, A., and Blanco, S. (2014). A gradient-enhanced large-deformation continuum damage model for fibre-reinforced materials. *Computer Methods in Applied Mechanics and Engineering*, 268:801–842.

- [111] Wang, Z., Shedbale, A. S., Kumar, S., and Poh, L. H. (2019). Localizing gradient damage model with micro inertia effect for dynamic fracture. *Computer Methods in Applied Mechanics and Engineering*, 355:492–512.
- [112] Weisło, B., Pamin, J., and Kowalczyk-Gajewska, K. (2013). Gradient-enhanced damage model for large deformations of elastic-plastic materials. *Archives of Mechanics*, 65(5):407–428.
- [113] Willam, K. and Warnke, E. (1975). Constitutive models for the triaxial behavior of concrete. In *Proceedings of the International Association for Bridge and Structural Engineering*, volume 19, pages 1–30, Bergamo, Italy.
- [114] Xotta, G., Beizae, S., and Willam, K. J. (2016). Bifurcation investigations of coupled damage-plasticity models for concrete materials. *Computer Methods in Applied Mechanics and Engineering*, 298:428–452.
- [115] Zreid, I. and Kaliske, M. (2018). A gradient enhanced plasticity–damage microplane model for concrete. *Computational Mechanics*, 62(5):1239–1257.

Declaration of interests

The authors declare that they have no known competing financial interests or personal relationships that could have appeared to influence the work reported in this paper.

The authors declare the following financial interests/personal relationships which may be considered as potential competing interests: